Uncertainty of thermosphere mass density observations derived from accelerometer and GNSS tracking data

Siemes, C.; van den IJssel, J.A.A.; Visser, P.N.A.M.

DOI
10.1016/j.asr.2024.02.057

Publication date
2024

Document Version
Final published version

Published in
Advances in Space Research

Available online at www.sciencedirect.com

ScienceDirect

Advances in Space Research 73 (2024) 5043–5063

ADVANCES IN SPACE RESEARCH (a COSPAR publication)

www.elsevier.com/locate/asr

Uncertainty of thermosphere mass density observations derived from accelerometer and GNSS tracking data

Christian Siemes *, Jose van den IJssel, Pieter Visser

Delft University of Technology, Kluyverweg 1, Delft 2629 HS, Netherlands

Received 21 January 2024; received in revised form 26 February 2024; accepted 28 February 2024
Available online 5 March 2024

Abstract

Thermosphere mass density and crosswind can be derived from accelerometer and GNSS tracking data. However, present datasets are often provided without comprehensive uncertainty specifications. We present a newly developed method that propagates measurement noise and errors in the satellite specification, thermosphere models, and radiation flux data to density observations to quantify their uncertainty. We focus specifically on density observations derived only from GNSS tracking data, which are limited in resolution along the orbit due to unavoidable smoothing. While the method can be applied to simulated and real data, making it useful for existing datasets and mission design, we demonstrated it using data from the GRACE B satellite. First, we compare the aerodynamic acceleration derived separately from the accelerometer and GNSS tracking data, highlighting the role of two significant noise sources: noise due to the differentiation of the positions and noise from the evaluation of the gravity vector at a noisy position. Averaging substantially reduces the noise in the aerodynamic acceleration as long as the differentiation noise dominates, which is the case at frequencies higher than the orbital frequency. Below, gravity vector evaluation noise becomes the dominating noise source, and consequently, averaging over longer periods leads to only marginal uncertainty reduction. Further, we investigate the uncertainty in the radiation pressure acceleration and demonstrate that averaging over one orbit substantially reduces the uncertainty in the along-track radiation pressure acceleration. We show that the uncertainty of density observations derived from the accelerometer data is about 4% of the density for data from 2003 when the GRACE B satellite was at 490 km altitude during high solar activity. In 2008, solar activity was very low, and the altitude was still 476 km, resulting in an uncertainty of 5%–20% because GNSS tracking noise and radiation pressure modeling errors play a much larger role as the aerodynamic acceleration becomes smaller. In the case of density observations derived only from GNSS tracking data, the uncertainty is about 5% in 2003 and 20%–50% in 2008 when averaging over one-third orbit. In 2008, GNSS tracking noise explains nearly all uncertainty in the density observation. Averaging over one orbit reduces the uncertainty to 4% and 5% in 2003 and 2008, respectively.

Keywords: Neutral density; Uncertainty; Accelerometer; GNSS tracking

1. Introduction

Accurate knowledge of thermosphere mass density is essential for orbit predictions at altitudes approximately below 600 km, which are key to collision risk assessment and avoidance, mission design and planning, and lifetime predictions. Deriving in situ observations of thermosphere mass density from precise accelerometer measurements is a well-established technique, which was used to generate several density datasets from the measurements of the CHAMP, GRACE, GOCE, and GRACE-FO satellites (Bruinsma and Biancale, 2003; Sutton et al., 2007; Bruinsma et al., 2014; Mehta et al., 2017; Siemes et al., 2023). Yet, the observational coverage is sparse because of the limited number of satellites featuring a precise

* Corresponding author.
E-mail address: c.siemes@tudelft.nl (C. Siemes).

https://doi.org/10.1016/j.asr.2024.02.057
0273-1177/

accelerometer (Bruinsma et al., 2022). More recently, GNSS tracking data have been used to derive in situ thermosphere mass density observations, albeit at a lower resolution along the orbit (van den IJssel et al., 2020). Despite its lower resolution, GNSS tracking data hold promise for drastically improving observational coverage as modern GNSS receivers are used on many satellites.

Density observations derived from accelerometer and GNSS tracking data are used for several purposes. The most obvious is the development of new thermosphere models, for instance, the DTM-2020 model (Bruinsma and Boniface, 2021). Further, density observations have been used for assessing, e.g., methods for assimilating density observations derived from radar tracking (Gondelach and Linares, 2021) and the SET HASDM density database (Licata et al., 2021). They have also been used for studying short periods with stronger than usual geomagnetic activity, where the density enhancement on 3–4 February 2023, which led to the loss of 38 Starlink satellites launched in that period, is a more recent example (He et al., 2023). Several authors investigated the assimilation of near-real-time density observations into models, although density observations derived from the accelerometer and GNSS tracking data have not yet been produced with sufficiently low latency (Codrescu et al., 2018; Sutton, 2018; Forootan et al., 2021).

Supplementing density observations with uncertainty estimates would be useful for all these applications, particularly for data assimilation. However, most currently available density observations are provided without uncertainty estimates, where the only exception known to us is the GOCE density dataset. For that dataset, the density observations' uncertainty is derived assuming an along-track acceleration accuracy of 0.5nm s^{-2}, noise in the ion thruster actuation, radiation pressure modeling errors, and wind model errors (Doornbos et al., 2014). However, this does not mean that the producers of the other density datasets have not investigated the uncertainty.

Most research focussed on the CHAMP satellite since it was the first of several geodetic satellites featuring a precise accelerometer. Bruinsma and Biancale (2003) evaluated how instrument noise and errors in the accelerometer data calibration, drag coefficient modeling, wind, satellite attitude, and satellite mass influence CHAMP density observations. They focused on September 2000 to May 2002, a period of high solar activity, and found an uncertainty of 10%–15%. Also, Sutton et al. (2007) and Doornbos et al. (2010) studied the uncertainty of CHAMP density observations considering a similar set of noise and error sources, coming to the same conclusion. Bruinsma et al. (2022) provide a comprehensive discussion of the error sources, which is not limited to the CHAMP satellite.

The drag coefficient modeling has been scrutinized in recent years. In the context of this paper, it is important to realize that an error in the drag coefficient results in an incorrect scaling of the density observations (Doornbos, 2011, Chap. 3). Mehta et al. (2022) discussed the impact of several drag coefficient modeling approaches for the CHAMP, GRACE, and GOCE satellites. While they found an agreement of the drag coefficients within a few percent for the CHAMP and GOCE satellites, the discrepancies reached 30% for the GRACE satellites in 2007–2010. During that period, solar activity was very low, and the satellite altitude was about 470 km. These results are consistent with those of Bernstein and Pilinski (2022), who investigated the uncertainty in the gas-surface interaction modeling, which underlies the drag coefficient modeling.

Assessing the uncertainty of density observations derived from GNSS tracking is more complex because it depends on the smoothing required to counter high-frequency noise. Van den IJssel et al. (2020) provide a conservative uncertainty assessment for the Swarm satellites. For April–July 2014, a period of high solar activity, they found an uncertainty of 4% for Swarm A and C, flying side-by-side at an altitude of about 480 km at that time. The uncertainty for Swarm B was 7% during the same period due to the higher altitude of 520 km. In April–July 2019, a period of low solar activity, the uncertainty increased to 19% for Swarm A and C and even 60% for Swarm B, noting that the altitude was then about 450 km for Swarm A and C and 510 km for Swarm B.

The abovementioned uncertainty quantifications have several shortcomings. While realistic errors were assumed for the accelerometer data calibration, the relation to the tracking performance of the GNSS receiver is unclear. Further, radiation pressure modeling errors were treated as a simple fraction of the radiation pressure acceleration, not depending on, e.g., the absorption and reflection properties of the satellite surfaces. Also, the acceleration due to the satellite's thermal emission was entirely neglected, and hence, the uncertainty due to this error source was not considered. In the case of density observations derived from GNSS tracking data, only empirical uncertainty assessments were carried out.

We present a method for comprehensive uncertainty quantification for density observations derived from accelerometer and GNSS tracking data. We consider the uncertainty in all input parameters in the derivation of the density observations and propagate that uncertainty to the density observations. In that process, we establish a clear link to the accuracy of the GNSS tracking. The method can be applied not only to real data but also to simulated data, i.e., the user may define the orbit and instrument accuracy of a hypothetical satellite mission to assess its capability of deriving density observations. This makes the method valuable for existing datasets and for predicting future missions' observational accuracy. We will demonstrate the tool for the GRACE satellites, which experienced solar maximum and minimum conditions at similar altitudes of 500 km and 480 km, respectively.

The paper is structured as follows. The method is presented in detail in Section 2 while Section 4 introduces the models utilized by the method. The GRACE B data

and the selection of test periods are presented in Section 5. Section 6 specifies the uncertainty of the input parameters of the uncertainty propagation. The results are presented and discussed in Section 7. We conclude in Section 8 and give an outlook to future work in Section 9.

2. Density derivation method

2.1. Derivation of density observations from accelerometer data

The motion of a satellite is governed by the total acceleration $\boldsymbol{a}_{\text{total}}$ along the orbit, which we can split into the gravitational acceleration $\boldsymbol{a}_{\text{grav}}$, the non-gravitational acceleration $\boldsymbol{a}_{\text{non-grav}}$, and the acceleration due to thruster activations:

$$\boldsymbol{a}_{\text{total}} = \boldsymbol{a}_{\text{grav}} + \boldsymbol{a}_{\text{non-grav}} + \boldsymbol{a}_{\text{thrust}} \tag{1}$$

We distinguish between continuous and impulsive thrusts, which require different handling. In the case of impulse thrust, thruster activations typically affect only a small fraction of the orbit and are easy to edit out. Continuous thrust, on the other hand, needs to be modeled and subtracted. The non-gravitational acceleration is composed of the aerodynamic acceleration $\boldsymbol{a}_{\text{aero}}$ and the radiation pressure acceleration $\boldsymbol{a}_{\text{rp}}$, i.e.

$$\boldsymbol{a}_{\text{non-grav}} = \boldsymbol{a}_{\text{aero}} + \boldsymbol{a}_{\text{rp}}, \tag{2}$$

where the latter comprises the effects from solar radiation (sr), albedo (alb), Earth's radiation (er), and the satellite's thermal emission (te):

$$\boldsymbol{a}_{\text{rp}} = \boldsymbol{a}_{\text{sr}} + \boldsymbol{a}_{\text{alb}} + \boldsymbol{a}_{\text{er}} + \boldsymbol{a}_{\text{te}} \tag{3}$$

An accelerometer placed in the satellite's center of mass will sense the non-gravitational acceleration. State-of-the-art accelerometers use electrostatic forces to control the position and orientation of a proof mass inside a cage (Touboul et al., 2012). Since these instruments are designed for the micro-gravity environment in space, they cannot be calibrated on the ground because the electrostatic forces are too small to lift the proof mass in the 1-g environment (Touboul et al., 2016). Therefore, we need to calibrate the measured acceleration $\boldsymbol{a}_{\text{meas,non-grav}}$ by applying a bias vector $\boldsymbol{b}$ and a scale factor matrix $\boldsymbol{S}$ to obtain the calibrated acceleration $\boldsymbol{a}_{\text{cal,non-grav}}$:

$$\boldsymbol{a}_{\text{cal,non-grav}} = \boldsymbol{S}\,\boldsymbol{a}_{\text{meas,non-grav}} + \boldsymbol{b} \tag{4}$$

Although some authors account for the misalignments of the accelerometer axes (Klinger and Mayer-Gürr, 2016), we consider only the accelerometer scale factors since the effect of misalignments on density observations is very small, i.e., $\boldsymbol{S}$ is a diagonal matrix in our case. The scale factors are nearly constant throughout the mission lifetime, whereas biases may exhibit drifts and temperature-driven changes at daily time scales (Klinger and Mayer-Gürr, 2016; Teixeira Da Encarnação et al., 2020; Siemes et al., 2023). The scale factors and biases are typically obtained by fitting the calibrated acceleration to GNSS tracking data using precise orbit determination (van Helleputte et al., 2009). Thus, the GNSS tracking accuracy is important for the accuracy of the calibrated acceleration, as further elaborated in Section 3.1.

We extract the aerodynamic acceleration by subtracting the modeled radiation pressure acceleration:

$$\boldsymbol{a}_{\text{aero}} = \boldsymbol{a}_{\text{cal,non-grav}} - \boldsymbol{a}_{\text{rp}} \tag{5}$$

The atmospheric mass density ρ is related to the aerodynamic acceleration by

$$\boldsymbol{a}_{\text{aero}} = -\frac{1}{2}\frac{\rho \mid \boldsymbol{v}_{\text{rel}} \mid^2}{m_{\text{sat}}}\boldsymbol{C}_{\text{aero}}, \tag{6}$$

where m_{sat} is the satellite's mass, $\boldsymbol{C}_{\text{aero}}$ is the aerodynamic coefficient vector intrinsically scaled by the cross-section area, and $\boldsymbol{v}_{\text{rel}}$ is the satellite's velocity relative to the atmosphere. The density is obtained by projecting Eq. (6) onto a suitable direction specified by unit vector $\hat{\boldsymbol{e}}$:

$$\rho = -2\frac{\boldsymbol{a}_{\text{aero}} \cdot \hat{\boldsymbol{e}}}{\boldsymbol{C}_{\text{aero}} \cdot \hat{\boldsymbol{e}}}\frac{m_{\text{sat}}}{\mid \boldsymbol{v}_{\text{rel}} \mid^2} \tag{7}$$

Logical choices are $\hat{\boldsymbol{e}} = \boldsymbol{v}_{\text{rel}}/\mid \boldsymbol{v}_{\text{rel}} \mid$ or setting $\hat{\boldsymbol{e}}$ equal to the accelerometer axis that is most closely aligned with $\boldsymbol{v}_{\text{rel}}$ (Doornbos, 2011; Mehta et al., 2022).

2.2. Derivation of density observations from GNSS tracking data

Density observations can be derived from GNSS tracking data by different methods. For instance, Calabia et al. (2015) use numerical differentiation based on Lagrangian interpolation of a precise orbit to obtain the total acceleration. Then, they subtract the modeled gravitational and radiation pressure accelerations to obtain the aerodynamic acceleration, which they convert to density observations. Van den IJssel et al. (2020) use a Kalman smoother to fit empirical accelerations to a precise orbit, where modeled gravitational and radiation pressure accelerations are part of the force model, allowing for the extraction of the aerodynamic acceleration. Both approaches require averaging of the aerodynamic acceleration, i.e., the methods yield the average aerodynamic acceleration $\bar{\boldsymbol{a}}_{\text{aero}}$ instead of the quasi-instantaneous aerodynamic acceleration $\boldsymbol{a}_{\text{aero}}$. The averaging is performed along the orbit and must be accounted for in uncertainty propagation. For the sake of simplicity, we assume an idealized lowpass filter with a sharp cutoff in the frequency domain, as further explained in Section 3.3.

2.3. Satellite model

In our method, the satellite geometry is represented by panels with given surface areas and outward-pointing normal vectors. Each panel is augmented with surface properties related to radiation pressure and gas-surface interaction. The properties are the absorption, diffuse and

specular reflection coefficients for visible light and infrared radiation, the heat capacity and conductivity toward the satellite body, and the energy accommodation coefficient that describes the momentum exchange between gas particles and the satellite surface. We assume that the energy accommodation coefficient is the same for all panels. The remaining satellite model parameters are the satellite mass, the inner body's heat capacitance, and the heat generation inside the satellite due to electronic components.

2.4. Aerodynamics

We choose the Diffuse Reflections with Incomplete Accommodation (DRIA) model for gas-surface interaction since it is reasonably accurate in the altitude range of interest, approximately from 200 km to 1000 km, and because of its simple analytic form when applied to a panel model of the satellite (Mehta et al., 2022; Bernstein and Pilinski, 2022). The model is based on the equations for a flat panel derived by Sentman (1961), with the modified expression for the velocity ratio of incident and reemitted particles derived by Koppenwallner (2009). The equations for calculating the aerodynamic coefficient vector are provided by, e.g., Doornbos (2011) and are repeated in Appendix A for convenience. The aerodynamic coefficient vector is a function of the panel areas A_i, the panel normals $\hat{\boldsymbol{n}}_i$, the panel temperatures T_i, the relative velocity vector $\boldsymbol{v}_{\mathrm{rel}}$, the atmospheric temperature T_{atm}, the atmospheric composition given by the mass density ρ_j per atmospheric constituent j, and the energy accommodation coefficient α_E, i.e. $\boldsymbol{C}_{\mathrm{aero}}(A_i, \hat{\boldsymbol{n}}_i, T_i, \boldsymbol{v}_{\mathrm{rel}}, T_{\mathrm{atm}}, \rho_j, \alpha_E)$.

2.5. Radiation pressure

We use a panel model of the satellite to calculate the radiation pressure as described by, e.g., Doornbos (2011). The acceleration due to any radiation source can be expressed as

$$\boldsymbol{a}_{\mathrm{src}} = -\frac{\Phi_{\mathrm{src}}}{m_{\mathrm{sat}} c} \sum_i A_i \gamma_i \left(c_{\mathrm{w,a},m} \hat{\boldsymbol{r}} + c_{\mathrm{w,d},m} (\hat{\boldsymbol{r}} + \frac{2}{3} \hat{\boldsymbol{n}}_i) + 2\gamma_i c_{\mathrm{w,s},m} \hat{\boldsymbol{n}}_i \right) \tag{8}$$

where the source indicated by subscript 'src' can be solar radiation, albedo, or Earth's radiation as in Eq. (3). The wavelength indicated by subscript 'w' can be visible light (vis) for solar radiation and albedo or infrared radiation (ir) for Earth's radiation. Further, Φ_{src} is the radiation flux, c is the speed of light, and

$$\gamma_i = \begin{cases} \hat{\boldsymbol{r}} \cdot \hat{\boldsymbol{n}}_i, & \hat{\boldsymbol{r}} \cdot \hat{\boldsymbol{n}}_i \geqslant 0 \\ 0, & \hat{\boldsymbol{r}} \cdot \hat{\boldsymbol{n}}_i < 0 \end{cases}, \tag{9}$$

where $\hat{\boldsymbol{r}}$ is a unit vector pointing from the satellite to the radiation source. Since we assign materials to panels, indicated by subscript m, we denote the absorption coefficient by $c_{\mathrm{w,a},m}$ and the diffuse and specular reflection coefficients by $c_{\mathrm{w,d},m}$ and $c_{\mathrm{w,s},m}$, respectively. The relation between the panel index i and the material index m is established by a lookup table. Assigning materials to panels is needed to account for the fact that radiation pressure acceleration errors of individual panels may, at least partially, cancel each other when the panels have the same material but a different orientation (e.g., the solar arrays of the GRACE satellites).

Calculating the radiation flux is straightforward for solar radiation:

$$\Phi_{\mathrm{sr}} = f_{\mathrm{sf}} \left(\frac{1\,\mathrm{AU}}{|\boldsymbol{r}_{\mathrm{sun}} - \boldsymbol{r}_{\mathrm{sat}}|} \right)^2 \Phi_{1\,\mathrm{AU}} \tag{10}$$

Here, $\boldsymbol{r}_{\mathrm{sun}}$ and $\boldsymbol{r}_{\mathrm{sat}}$ are the position of the Sun and the satellite, respectively, $\Phi_{1\,\mathrm{AU}} = 1367\mathrm{Wm}^{-2}$ is the solar radiation flux at a distance of one astronomical unit (1 AU), and f_{sf} is the shadow function. The latter ranges from 0, when the satellite is inside Earth's umbra, to 1 when the satellite is in full sunlight. We use the Solar radiation pressure with Oblateness and Lower Atmospheric Absorption, Refraction, and Scattering Curve Fit (SOLAARS-CF) shadow function developed by Robertson (2015).

The calculation of the radiation fluxes due to albedo and Earth's radiation is more complex. In brief, we subdivide Earth's surface into a grid and perform the calculations for each grid cell separately. For albedo, we first calculate the radiation flux received by the k-th grid cell considering the angle of incidence. Then, we reduce the received radiation flux by the albedo factor of the grid cell and calculate the reflected radiation flux $\Phi_{\mathrm{alb},k}$ in the direction of the satellite, assuming a diffuse reflection, i.e. Lambert's cosine law. For Earth's radiation, each grid cell represents the emitted radiation flux. Thus, we calculate the radiation flux of the k-th grid cell, $\Phi_{\mathrm{er},k}$, in the direction of the satellite according to diffuse emission. We refer to Doornbos et al. (2014) for a detailed description of the calculations.

2.6. Thermal emission

The satellite's thermal emission can be calculated using a panel model, as described by Siemes et al. (2023). In that model, the panels gain heat by absorbing incident radiation, exchange heat with the satellite body via conduction, and emit heat to cold space. In addition, the satellite body generates heat because a fraction of the electric power is converted to heat by the onboard electrical systems. This leads to the heat changes $\dot{Q}_i$ and $\dot{Q}_{\mathrm{body}}$ of the i-th panel and the satellite body, respectively. These heat changes are determined at every time step t_n to update the panels' and body's absolute temperatures T_i and T_{body}, respectively, of the next time step t_{n+1}, using the discretised equations

$$T_i(t_{n+1}) = T_i(t_n) + \frac{\dot{Q}_i}{C_i} (t_{n+1} - t_n) \tag{11}$$

and

$$T_{\text{body}}(t_{n+1}) = T_{\text{body}}(t_n) + \frac{\dot{Q}_{\text{body}}}{C_{\text{body}}}(t_{n+1} - t_n), \tag{12}$$

where C_i and C_{body} are the heat capacitances of the i-th panel and the satellite body. The acceleration due to the satellite's thermal emission is

$$\boldsymbol{a}_{\text{te}} = -\frac{2}{3}\sum_i \frac{\dot{Q}_{\text{emit},i}}{m_{\text{sat}}\, c}\hat{\boldsymbol{n}}_i, \tag{13}$$

where $\dot{Q}_{\text{emit},i}$ is the heat emitted by the i-th panel. According to the Stefan–Boltzmann law,

$$\dot{Q}_{\text{emit},i} = A_i \varepsilon_i \sigma T_i^4, \tag{14}$$

where ε_i is the panel's emissivity and σ is the Stefan–Boltzmann constant. The emissivity is equal to the absorption coefficient, i.e. $\varepsilon_i = c_{\text{ir,a},m}$, where we need the look-up table relating the i-th panel to the m-th material to select the correct coefficient.

From Section 2.5 and 2.6, it is clear that the radiation pressure acceleration is a function of the time steps, satellite mass, panel areas and normals, absorption and reflection coefficients, radiation fluxes, and panel temperatures, i.e. $\boldsymbol{a}_{\text{rp}}(t_n, m_{\text{sat}}, A_i, \hat{\boldsymbol{n}}_i, c_{\text{vis,a},m}, c_{\text{vis,d},m}, c_{\text{vis,s},m}, c_{\text{ir,a},m}, c_{\text{ir,d},m}, c_{\text{ir,s},m}, \Phi_{\text{sr}}, \Phi_{\text{alb},k}, \Phi_{\text{er},k}, T_i(t_n))$. In turn, the panel temperatures are a function of the time steps, the previous temperature of the panels and the satellite body, panels heat capacitances and conductivities to the satellite body, heat generation of the satellite body, panel areas and normals, absorption coefficients for visible light and infrared radiation, and radiation fluxes, i.e. $T_i(t_{n+1}, T_i(t_n), T_{\text{body}}(t_n), C_i, C_{\text{body}}, k_i, \dot{Q}_{\text{gen}}, A_i, \hat{\boldsymbol{n}}_i, c_{\text{ir,a},m}, c_{\text{vis,a},i}, \Phi_{\text{sr}}, \Phi_{\text{alb},k}, \Phi_{\text{er},k})$, where k_i is the heat conductivity of the i-th panel and $\dot{Q}_{\text{gen}}$ is the heat generation of the satellite body.

3. Uncertainty propagation method

We consider that the output parameter vector $\boldsymbol{y}$ is a nonlinear function of the input parameter vector $\boldsymbol{x}$, i.e., $\boldsymbol{y} = \boldsymbol{f}(\boldsymbol{x})$. In our case, the output parameter is the density observation, while the input parameters are the panel areas, the reflection coefficients, etc. Since uncertainty propagation requires a linear relationship, we expand the nonlinear function $\boldsymbol{f}(\boldsymbol{x})$ in a Taylor series truncated after the linear term:

$$\boldsymbol{f}(\boldsymbol{x}) = \boldsymbol{f}(\boldsymbol{x}_0) + \boldsymbol{J}\Delta\boldsymbol{x} + O(\Delta\boldsymbol{x}^2) \approx \boldsymbol{f}(\boldsymbol{x}_0) + \boldsymbol{J}\Delta\boldsymbol{x}, \tag{15}$$

Here, we assume that the higher order terms $O(\Delta\boldsymbol{x}^2)$ are negligible when $\boldsymbol{x}$ is close to the Taylor point $\boldsymbol{x}_0$ since then $\Delta\boldsymbol{x} = \boldsymbol{x} - \boldsymbol{x}_0$ is small. Further, $\boldsymbol{J} = \partial\boldsymbol{f}/\partial\boldsymbol{x}|_{\boldsymbol{x}=\boldsymbol{x}_0}$ is the Jacobian matrix evaluated at the Taylor point. The covariance matrix of the output parameter vector is

$$\Sigma_{\boldsymbol{y}} = \boldsymbol{J}\Sigma_{\boldsymbol{x}}\boldsymbol{J}^T, \tag{16}$$

where $\Sigma_{\boldsymbol{x}}$ is the covariance matrix of input parameter vector. In the following subsections, we explain how we apply Eq. (16) to obtain the density observations' uncertainty.

3.1. Accuracy of accelerometer measurements

Accelerometer measurements exhibit colored noise (Touboul et al., 2016), best described by the Power Spectral Density (PSD) of the noise. The PSD can be regarded as the variance per frequency, where the integral over the PSD gives the variance in the time domain according to Parseval's theorem (Smith, 2003, Chap. 10). As described in Section 2.1, accelerometer measurements are calibrated using GNSS tracking data. Particularly, the low-frequency content of the accelerometer data is adjusted by the bias. Therefore, we define the variance of the accelerometer noise as

$$\sigma^2_{\text{acc}} = 2\int_{f_b}^{\frac{f_s}{2}} P_{\text{acc}}(f)\, df, \tag{17}$$

where f_b is the frequency of the bias estimation, f_s is the sampling frequency, and $P_{\text{acc}}(f)$ is the PSD of the accelerometer noise, which is a function of frequency f. In principle, we must integrate from f_b to $f_s/2$ and from $-f_s/2$ to $-f_b$ to obtain the variance, where $f_s/2$ is the Nyquist frequency. However, we can simplify by integrating from f_b to $f_s/2$ and multiplying by 2 since the PSD is an even function of frequency.

The accelerometers measure the acceleration not equally accurate in all directions. Typically, one of the directions is less sensitive and, consequently, noisier due to the design of the accelerometers, which allows for some ground testing (Touboul et al., 2012). Therefore, we define the covariance matrix of the calibrated accelerations as

$$\Sigma_{\text{acc}} = \begin{bmatrix} \sigma^2_{\text{acc,x}} & 0 & 0 \\ 0 & \sigma^2_{\text{acc,y}} & 0 \\ 0 & 0 & \sigma^2_{\text{acc,z}} \end{bmatrix}, \tag{18}$$

where the variances on the diagonal follow from Eq. (17), using the noise PSD of the sensitive and less sensitive accelerometer measurement directions.

3.2. Accuracy of GNSS tracking data

Often, we know the variance of the position noise, e.g. from the specification of the GNSS receiver or orbit validation via ground-to-satellite laser ranging. Further, position noise can exhibit time correlations, which is evident from comparing the orbit calculated by a GNSS receiver onboard to a precise orbit calculated on the ground or from comparing accelerations derived from GNSS tracking to accelerometer data. Therefore, we define the PSD of the position noise as

$$P_{\text{pos}}(f) = c f^{2\alpha}, \tag{19}$$

where the term $f^{2\alpha}$ accounts for time correlations and the constant c is related to the position noise variance. Parameter α defines the slope of the PSD in the logarithmic domain. As in Section 3.1, we find the position noise vari-

ance σ^2_{pos} by calculating the area under the PSD. However, here we integrate from frequency $f = 0$ to the Nyquist frequency $f_s/2$:

$$\sigma^2_{\text{pos}} = 2\int_0^{\frac{f_s}{2}} cf^{2\alpha} df = \frac{2c}{2\alpha+1} f_s^{2\alpha+1} \tag{20}$$

By rearranging this equation, we find

$$c = \sigma^2_{\text{pos}} \frac{2\alpha+1}{2f_s^{2\alpha+1}}. \tag{21}$$

Thus, by specifying σ^2_{pos} and α, we define the PSD of the position noise. Further, by combining Eqs. (19) and (21), we find that only $\alpha > -0.5$ is a valid specification because the PSD must be positive.

Since the x, y, and z components of the position noise can be correlated, we define the position noise covariance matrix as

$$\Sigma_{\text{pos}} = \begin{bmatrix} \sigma^2_{\text{pos,x}} & \sigma_{\text{pos,xy}} & \sigma_{\text{pos,xz}} \\ \sigma_{\text{pos,xy}} & \sigma^2_{\text{pos,y}} & \sigma_{\text{pos,yz}} \\ \sigma_{\text{pos,xz}} & \sigma_{\text{pos,yz}} & \sigma^2_{\text{pos,z}} \end{bmatrix}. \tag{22}$$

The covariances $\sigma_{\text{pos,xy}}, \sigma_{\text{pos,xz}}$, and $\sigma_{\text{pos,yz}}$ follow from specifying the variances $\sigma^2_{\text{pos,x}}, \sigma^2_{\text{pos,y}}$, and $\sigma^2_{\text{pos,z}}$ and the correlations $\rho_{\text{pos,xy}}, \rho_{\text{pos,xz}}$, and $\rho_{\text{pos,yz}}$, and inserting the specified values in $\sigma_{\text{pos,ij}} = \rho_{\text{pos,ij}}\sigma_{\text{pos,i}}\sigma_{\text{pos,j}}$ for $\text{ij} \in \{\text{xy}, \text{xz}, \text{yz}\}$.

3.3. Differentiation of positions

Accelerations derived from GNSS tracking data are conceptually the second derivative of the positions with respect to time. Thus, we obtain the PSD of the acceleration noise by multiplying the PSD of the position noise by $(2\pi f)^4$. Assuming that the position noise is approximately white noise ($\alpha \approx 0$), the acceleration noise PSD will be small at low frequencies and large at high frequencies. Therefore, we apply lowpass filtering to counter the noise at high frequencies. Assuming a lowpass filter with a cutoff frequency f_u, we obtain the variance of the accelerations derived from GNSS tracking data due to differentiation by

$$\begin{aligned}\sigma^2_{\text{diff}} &= 2\int_0^{f_u} (2\pi f)^4 P_{\text{pos}}(f)\, df = 32c\pi^4 \int_0^{f_u} f^{2\alpha+4} df \\ &= \frac{32c\pi^4}{2\alpha+5} f_u^{2\alpha+5} = 16\pi^4 \sigma^2_{\text{pos}} \frac{2\alpha+1}{2\alpha+5} \frac{f_u^{2\alpha+5}}{f_s^{2\alpha+1}}.\end{aligned} \tag{23}$$

To select the cutoff frequency f_u, we consider two cases. The first is deriving density observations from accelerometer data, where the GNSS tracking is used to estimate the bias. Here, the cutoff frequency is equal to the frequency of the bias estimation, i.e., $f_u = f_b$. We define the period $T_b = f_b^{-1}$ of the bias estimation, where a typical value is $T_b = 1\text{d}$, i.e., biases are estimated daily (van Helleputte et al., 2009; Siemes et al., 2023). The second case is deriving density observations from GNSS tracking data only, where the selection of the cutoff frequency will depend on the signal-to-noise ratio. Since the cutoff frequency will limit the achievable resolution along the orbit and imply the level of averaging inherent to the lowpass filtering, we set $f_u = f_a$, where $T_a = f_a^{-1}$ is the averaging period. Van den IJssel et al. (2020) report a value of $T_a \approx 20\,\text{min}$ for the Swarm satellites.

As discussed in Section 3.1, the x, y, and z components of the position noise can be correlated, leading to correlated acceleration components. We account for correlations between the acceleration components by defining the covariance matrix of the acceleration noise as

$$\Sigma_{\text{diff}}(f_u) = \begin{bmatrix} \sigma^2_{\text{diff,x}} & \sigma_{\text{diff,xy}} & \sigma_{\text{diff,xz}} \\ \sigma_{\text{diff,xy}} & \sigma^2_{\text{diff,y}} & \sigma_{\text{diff,yz}} \\ \sigma_{\text{diff,xz}} & \sigma_{\text{diff,yz}} & \sigma^2_{\text{diff,z}} \end{bmatrix}, \tag{24}$$

where the covariances $\sigma_{\text{diff,xy}}, \sigma_{\text{diff,xz}}$, and $\sigma_{\text{diff,yz}}$ follow from inserting the variances from Eq. (23) and the correlations $\rho_{\text{diff,xy}} = \rho_{\text{pos,xy}}, \rho_{\text{diff,xz}} = \rho_{\text{pos,xz}}$, and $\rho_{\text{diff,yz}} = \rho_{\text{pos,yz}}$ in $\sigma_{\text{diff,ij}} = \rho_{\text{diff,ij}}\sigma_{\text{diff,i}}\sigma_{\text{diff,j}}$ for $\text{ij} \in \{\text{xy}, \text{xz}, \text{yz}\}$. Note that we express the covariance matrix as a function of the upper frequency f_u to distinguish between the two cases using f_b and f_a.

3.4. Gravity vector evaluation

GNSS tracking noise does not only propagate to acceleration noise via differentiation as described in Section 3.3 but also via the position at which the gravitational acceleration Eq. (1) is evaluated. In the latter case, the position noise propagates to the aerodynamic acceleration largely via the term

$$\boldsymbol{a}_{\text{grav}} = -\frac{GM}{|\boldsymbol{r}|^3}\boldsymbol{r}, \tag{25}$$

where $\boldsymbol{r}$ is the position vector and GM is the gravitational parameter. Higher-order terms of gravity field models have a negligible effect on the uncertainty propagation. The Jacobian matrix is

$$\boldsymbol{J}_{\text{grav}} = \frac{\partial \boldsymbol{a}_{\text{grav}}}{\partial \boldsymbol{r}} = -\frac{GM}{|\boldsymbol{r}|^5}\left(|\boldsymbol{r}|^2 \boldsymbol{I}_{3\times 3} - \boldsymbol{r}\boldsymbol{r}^T\right), \tag{26}$$

where $\boldsymbol{I}_{3\times 3}$ denotes an identity matrix of size 3×3. As described in Section 3, we obtain the covariance matrix of the gravity vector noise by

$$\Sigma_{\text{grav}} = \boldsymbol{J}_{\text{grav}} \Sigma_{\text{pos}} \boldsymbol{J}^T_{\text{grav}}, \tag{27}$$

where Σ_{pos} is the position noise covariance matrix defined in Eq. (22). This equation assumes a pointwise evaluation of the gravitational acceleration. To account for averaging over a window of length T_u, we rescale

$$\Sigma_{\text{grav}}(T_u) = \frac{T_s}{T_u}\Sigma_{\text{grav}}, \tag{28}$$

where T_s is the sampling frequency. We choose $T_u = T_a$ for GNSS tracking and $T_u = T_b$ for the accelerometer data due to the bias estimation (cf. Section 3.3).

3.5. Uncertainty propagation for radiation pressure and density

The uncertainty propagation was developed as a two-step procedure. First, we calculate the uncertainty of the sum of the radiation pressure and satellite thermal emission accelerations, accounting for correlations between the radiation pressure and satellite thermal modeling due to common input parameters (e.g., the absorption coefficients). Second, we propagate the uncertainty of the accelerometer and GNSS tracking data, combined radiation pressure and satellite thermal emission accelerations, aerodynamic modeling, relative velocity vector, and the thermosphere model to density observations. Since the linearisation is straightforward and unambiguous, we will focus on how the covariance matrices are structured in the following sections.

3.5.1. Uncertainty propagation for radiation pressure

We collect the input parameters (cf. Section 3) for the radiation pressure and satellite thermal modeling (cf. Section 2.5 and 2.6) in vector $\boldsymbol{x}_{\mathrm{rp},n}$, which we split into two subvectors:

$$\boldsymbol{x}_{\mathrm{rp},n} = \begin{bmatrix} \boldsymbol{x}_{\mathrm{rp},1,n} \\ \boldsymbol{x}_{\mathrm{rp},2,n} \end{bmatrix}. \tag{29}$$

The first subvector $\boldsymbol{x}_{\mathrm{rp},1}$ contains the

- panel temperatures $T_i(t_n)$,
- satellite body temperature $T_{\mathrm{body}}(t_n)$,
- materials' absorption and reflection coefficients $c_{\mathrm{vis,a},m}, c_{\mathrm{vis,d},m}, c_{\mathrm{vis,s},m}, c_{\mathrm{ir,a},m}, c_{\mathrm{ir,d},m}$, and $c_{\mathrm{ir,s},m}$,
- panel areas A_i,
- panels' heat conductivities to the satellite body k_i,
- panels' heat capacitances C_i,
- satellite mass m_{sat},
- satellite body's heat capacitance C_{body}, and
- satellite body's heat generation $\dot{Q}_{\mathrm{gen}}$.

We do not currently model the uncertainty in the panel normals and the satellite attitude. These omissions are motivated by the fact that the uncertainty in the panel orientation can, at least partially, be accounted for by the uncertainty in the panel area, and star sensors measure the satellite attitude highly accurately. The second subvector $\boldsymbol{x}_{\mathrm{rp},2,n}$ contains the solar radiation flux $\Phi_{\mathrm{sr}}(t_n)$, radiation flux $\Phi_{\mathrm{alb},k}(t_n)$ due to albedo, and Earth radiation flux $\Phi_{\mathrm{er},k}(t_n)$. The covariance matrix of the input parameters is structured according to the subdivision of vector $\boldsymbol{x}_{\mathrm{rp},n}$, i.e.

$$\boldsymbol{\Sigma}_{\boldsymbol{x}_{\mathrm{rp},n}} = \begin{bmatrix} \boldsymbol{\Sigma}_{\boldsymbol{x}_{\mathrm{rp},1,n}} & \boldsymbol{0} \\ \boldsymbol{0} & \boldsymbol{\Sigma}_{\boldsymbol{x}_{\mathrm{rp},2,n}} \end{bmatrix}, \tag{30}$$

where $\boldsymbol{0}$ denotes a matrix filled with zeros. This approach allows for accounting for correlations between temperatures $T_i(t_n)$ and the absorption coefficients $c_{\mathrm{vis,a},m}$ and $c_{\mathrm{ir,a},m}$, while keeping the computational effort due to large size of $\boldsymbol{\Sigma}_{\boldsymbol{x}_{\mathrm{rp},2,n}}$ reasonable. One could argue that the panel temperatures are correlated to the radiation fluxes. Nevertheless, we neglect those correlations to facilitate much faster calculations, benefitting from the zero off-diagonal blocks of $\boldsymbol{\Sigma}_{\boldsymbol{x}_{\mathrm{rp},n}}$. We expect that this simplification has no significant effect on the results.

Before proceeding with defining the output vector, let us clarify several choices. In principle, the satellite mass m_{sat} and satellite body's heat generation $\dot{Q}_{\mathrm{gen}}$ change over time. However, we assume that the error in these quantities is the same for all epochs, like an offset that applies to all epochs. At the present stage of development, we do not consider uncertainty in the panel normals but instead assign all uncertainty from the satellite geometry to the panel areas. Further, we express the standard deviation of the radiation fluxes $\Phi_{\mathrm{sr}}(t_n), \Phi_{\mathrm{alb},k}(t_n)$, and $\Phi_{\mathrm{er},k}(t_n)$ as a fraction of the signal, e.g. $\sigma_{\Phi_{\mathrm{sr}}(t_n)} = f_{\Phi_{\mathrm{sr}}} \Phi_{\mathrm{sr}}(t_n)$ with fraction $f_{\Phi_{\mathrm{sr}}} > 0$, as this conveniently takes into account that the radiation fluxes due to albedo and Earth radiation from distant surface elements will be small. Finally, we initialize $\boldsymbol{\Sigma}_{\boldsymbol{x}_{\mathrm{rp},n}}$ at epoch t_0 as a diagonal matrix based on user-specified variances of all input parameters.

The output vector $\boldsymbol{y}_{\mathrm{rp},n}$ of the uncertainty propagation contains the radiation pressure acceleration $\boldsymbol{a}_{\mathrm{rp}}(t_n)$ and the input vector $\boldsymbol{x}_{\mathrm{rp},1,n+1}$ for the next epoch. However, instead of splitting the output vector $\boldsymbol{y}_{\mathrm{rp},n}$ into subvectors $\boldsymbol{a}_{\mathrm{rp}}(t_n)$ and $\boldsymbol{x}_{\mathrm{rp},1,n+1}$, it is more advantageous to split it into two subvectors in a different way that gives direct access to the covariance matrix of the radiation pressure acceleration, satellite panel and body temperatures so that correlations between these parameters are accounted for:

$$\boldsymbol{y}_{\mathrm{rp},n} = \begin{bmatrix} \boldsymbol{y}_{\mathrm{rp},1,n} \\ \boldsymbol{y}_{\mathrm{rp},2,n} \end{bmatrix} \tag{31}$$

Subvector $\boldsymbol{y}_{\mathrm{rp},1}$ contains the radiation pressure acceleration $\boldsymbol{a}_{\mathrm{rp}}(t_n)$, the panel temperatures $T_i(t_{n+1})$, and the satellite body temperature $T_{\mathrm{body}}(t_{n+1})$, while subvector $\boldsymbol{y}_{\mathrm{rp},2,n}$ comprises the

- absorption and reflection coefficients $c_{\mathrm{vis,a},m}, c_{\mathrm{vis,d},m}, c_{\mathrm{vis,s},m}, c_{\mathrm{ir,a},m}, c_{\mathrm{ir,d},m}$, and $c_{\mathrm{ir,s},m}$,
- panel areas A_i,
- panel heat conductivities k_i,
- panel heat capacitances C_i,
- satellite mass m_{sat},
- heat capacitance of the satellite body C_{body}, and
- heat generation $\dot{Q}_{\mathrm{gen}}$.

As before, we presently do not model the uncertainty in the panel normals and the satellite attitude.

With these definitions of the input and output vectors, we obtain the Jacobian matrix

$$\boldsymbol{J}_{\mathrm{rp},n} = \begin{bmatrix} \boldsymbol{J}_{\mathrm{rp},11,n} & \boldsymbol{J}_{\mathrm{rp},12,n} \\ \boldsymbol{J}_{\mathrm{rp},21,n} & \boldsymbol{J}_{\mathrm{rp},22,n} \end{bmatrix} = \begin{bmatrix} \partial \boldsymbol{y}_{\mathrm{rp},1,n}/\partial \boldsymbol{x}_{\mathrm{rp},1,n} & \partial \boldsymbol{y}_{\mathrm{rp},1,n}/\partial \boldsymbol{x}_{\mathrm{rp},2,n} \\ \partial \boldsymbol{y}_{\mathrm{rp},2,n}/\partial \boldsymbol{x}_{\mathrm{rp},1,n} & \partial \boldsymbol{y}_{\mathrm{rp},2,n}/\partial \boldsymbol{x}_{\mathrm{rp},2,n} \end{bmatrix}. \tag{32}$$

Since the reflection coefficients, etc., do not depend on the radiation fluxes, $\boldsymbol{J}_{\mathrm{rp},22,\mathrm{n}} = \boldsymbol{0}$. Applying the uncertainty propagation as in Eq. (16), we find

$$\Sigma_{\boldsymbol{y}_{\mathrm{rp},n}} = \begin{bmatrix} \boldsymbol{J}_{\mathrm{rp},11,n}\Sigma_{\boldsymbol{x}_{\mathrm{rp},1,n}}\boldsymbol{J}^T_{\mathrm{rp},11,n} + \boldsymbol{J}_{\mathrm{rp},12,n}\Sigma_{\boldsymbol{x}_{\mathrm{rp},2,n}}\boldsymbol{J}^T_{\mathrm{rp},12,n} & \boldsymbol{J}_{\mathrm{rp},11,n}\Sigma_{\boldsymbol{x}_{\mathrm{rp},1,n}}\boldsymbol{J}^T_{\mathrm{rp},21,n} \\ \boldsymbol{J}_{\mathrm{rp},21,n}\Sigma_{\boldsymbol{x}_{\mathrm{rp},1,n}}\boldsymbol{J}^T_{\mathrm{rp},11,n} & \boldsymbol{J}_{\mathrm{rp},21,n}\Sigma_{\boldsymbol{x}_{\mathrm{rp},1,n}}\boldsymbol{J}^T_{\mathrm{rp},21,n} \end{bmatrix}. \tag{33}$$

The matrix product $\boldsymbol{J}_{\mathrm{rp},12,n}\Sigma_{\mathrm{rp},2,n}\boldsymbol{J}^T_{\mathrm{rp},12,n}$ can be calculated efficiently despite the large size of $\Sigma_{\boldsymbol{x}_{\mathrm{rp},2,n}}$ by exploiting that the latter is a diagonal matrix. Further, $\Sigma_{\boldsymbol{y}_{\mathrm{rp},n}}$ contains $\Sigma_{\boldsymbol{x}_{\mathrm{rp},1,n+1}}$, including correlations between temperatures of epoch t_{n+1} and other input parameters in $\boldsymbol{x}_{\mathrm{rp},1,n+1}$, which we use to construct input parameter covariance matrix for the next epoch t_{n+1}.

Until this point, we described how to calculate the covariance matrix of the radiation pressure acceleration $\boldsymbol{a}_{\mathrm{rp},n}$. In the case of density observations derived from GNSS tracking data, we need to account for averaging. Assuming an average over $2L+1$ epochs gives the average radiation pressure acceleration

$$\bar{\boldsymbol{a}}_{\mathrm{rp},n} = \frac{1}{2L+1}\sum_{l=-L}^{L}\boldsymbol{a}_{\mathrm{rp},n+l}. \tag{34}$$

To arrive at a convenient formulation for the uncertainty propagation, we subdivide vector $\boldsymbol{x}_{\mathrm{rp},1,n}$ into two vectors:

$$\boldsymbol{x}_{\mathrm{rp},1,n} = \begin{bmatrix} \boldsymbol{x}_{\mathrm{rp},1\mathrm{a},n} \\ \boldsymbol{x}_{\mathrm{rp},1\mathrm{b}} \end{bmatrix} \tag{35}$$

Vector $\boldsymbol{x}_{\mathrm{rp},1\mathrm{a},n}$ contains the time-dependent temperatures $T_i(t_n)$ and $T_{\mathrm{body}}(t_n)$ and vector $\boldsymbol{x}_{\mathrm{rp},1\mathrm{b}}$ the other parameters of $\boldsymbol{x}_{\mathrm{rp},1,n}$. Then, the Jacobian matrix of $\bar{\boldsymbol{a}}_{\mathrm{rp},n}$ is

$$\bar{\boldsymbol{J}}_{\mathrm{rp},n} = \frac{1}{2L+1}\begin{bmatrix}\boldsymbol{I}_{3\times3} & \cdots & \boldsymbol{I}_{3\times3}\end{bmatrix}\begin{bmatrix} \frac{\partial \boldsymbol{a}_{\mathrm{rp},n-L}}{\boldsymbol{x}_{\mathrm{rp},1\mathrm{a},n-L}} & \boldsymbol{0} & \cdots & \boldsymbol{0} & \frac{\partial \boldsymbol{a}_{\mathrm{rp},n-L}}{\boldsymbol{x}_{\mathrm{rp},1\mathrm{b}}} & \frac{\partial \boldsymbol{a}_{\mathrm{rp},n-L}}{\boldsymbol{x}_{\mathrm{rp},2,n-L}} & \boldsymbol{0} & \cdots & \boldsymbol{0} \\ \boldsymbol{0} & \frac{\partial \boldsymbol{a}_{\mathrm{rp},n-L+1}}{\boldsymbol{x}_{\mathrm{rp},1\mathrm{a},n-L+1}} & \cdots & \boldsymbol{0} & \frac{\partial \boldsymbol{a}_{\mathrm{rp},n-L+1}}{\boldsymbol{x}_{\mathrm{rp},1\mathrm{b}}} & \boldsymbol{0} & \frac{\partial \boldsymbol{a}_{\mathrm{rp},n-L+1}}{\boldsymbol{x}_{\mathrm{rp},2,n-L+1}} & \cdots & \boldsymbol{0} \\ \vdots & \vdots & \ddots & \vdots & \vdots & \vdots & \vdots & \ddots & \vdots \\ \boldsymbol{0} & \boldsymbol{0} & \cdots & \frac{\partial \boldsymbol{a}_{\mathrm{rp},n+L}}{\boldsymbol{x}_{\mathrm{rp},1\mathrm{a},n+L}} & \frac{\partial \boldsymbol{a}_{\mathrm{rp},n+L}}{\boldsymbol{x}_{\mathrm{rp},1\mathrm{b}}} & \boldsymbol{0} & \boldsymbol{0} & \cdots & \frac{\partial \boldsymbol{a}_{\mathrm{rp},n+L}}{\boldsymbol{x}_{\mathrm{rp},2,n+L}} \end{bmatrix}. \tag{36}$$

The covariance matrix of the input parameter vector is

$$\bar{\Sigma}_{\boldsymbol{x}_{\mathrm{rp},n}} = \begin{bmatrix} \Sigma_{\boldsymbol{x}_{\mathrm{rp},1\mathrm{a},n-L}} & \boldsymbol{0} & \cdots & \boldsymbol{0} & \Sigma_{\boldsymbol{x}_{\mathrm{rp},1\mathrm{a},n-L},\boldsymbol{x}_{\mathrm{rp},1\mathrm{b}}} & \boldsymbol{0} & \boldsymbol{0} & \cdots & \boldsymbol{0} \\ \boldsymbol{0} & \Sigma_{\boldsymbol{x}_{\mathrm{rp},1\mathrm{a},n-L+1}} & \cdots & \boldsymbol{0} & \Sigma_{\boldsymbol{x}_{\mathrm{rp},1\mathrm{a},n-L+1},\boldsymbol{x}_{\mathrm{rp},1\mathrm{b}}} & \boldsymbol{0} & \boldsymbol{0} & \cdots & \boldsymbol{0} \\ \vdots & \vdots & \ddots & \vdots & \vdots & \vdots & \vdots & & \vdots \\ \boldsymbol{0} & \boldsymbol{0} & \cdots & \Sigma_{\boldsymbol{x}_{\mathrm{rp},1\mathrm{a},n+L}} & \Sigma_{\boldsymbol{x}_{\mathrm{rp},1\mathrm{a},n+L},\boldsymbol{x}_{\mathrm{rp},1\mathrm{b}}} & \boldsymbol{0} & \boldsymbol{0} & \cdots & \boldsymbol{0} \\ \Sigma_{\boldsymbol{x}_{\mathrm{rp},1\mathrm{b}},\boldsymbol{x}_{\mathrm{rp},1\mathrm{a},n-L}} & \Sigma_{\boldsymbol{x}_{\mathrm{rp},1\mathrm{b}},\mathrm{rp},1\mathrm{a},n-L+1} & \cdots & \Sigma_{\boldsymbol{x}_{\mathrm{rp},1\mathrm{b}},\mathrm{rp},1\mathrm{a},n+L} & \Sigma_{\boldsymbol{x}_{\mathrm{rp},1\mathrm{b}}} & \boldsymbol{0} & \boldsymbol{0} & \cdots & \boldsymbol{0} \\ \boldsymbol{0} & \boldsymbol{0} & \cdots & \boldsymbol{0} & \boldsymbol{0} & \Sigma_{\boldsymbol{x}_{\mathrm{rp},2,n-L}} & \boldsymbol{0} & \cdots & \boldsymbol{0} \\ \boldsymbol{0} & \boldsymbol{0} & \cdots & \boldsymbol{0} & \boldsymbol{0} & \boldsymbol{0} & \Sigma_{\boldsymbol{x}_{\mathrm{rp},2,n-L+1}} & \cdots & \boldsymbol{0} \\ \vdots & \vdots & & \vdots & \vdots & \vdots & \vdots & \ddots & \vdots \\ \boldsymbol{0} & \boldsymbol{0} & \cdots & \boldsymbol{0} & \boldsymbol{0} & \boldsymbol{0} & \boldsymbol{0} & \cdots & \Sigma_{\boldsymbol{x}_{\mathrm{rp},2,n+L}} \end{bmatrix}, \tag{37}$$

noting that all elements of this matrix are available from the calculation of covariance matrices $\Sigma_{\boldsymbol{y}_{\mathrm{rp},n-L}}$, $\Sigma_{\boldsymbol{y}_{\mathrm{rp},n-L+1}}, \ldots, \Sigma_{\boldsymbol{y}_{\mathrm{rp},n+L}}$. Applying the uncertainty propagation yields the covariance matrix of the average radiation pressure acceleration:

$$\Sigma_{\bar{\boldsymbol{a}}_{\mathrm{rp},n}} = \bar{\boldsymbol{J}}_{\mathrm{rp},n} \bar{\Sigma}_{\boldsymbol{x}_{\mathrm{rp},n}} \bar{\boldsymbol{J}}^T_{\mathrm{rp},n} \tag{38}$$

Obviously, we can exploit the sparseness of the matrices $\bar{\boldsymbol{J}}_{\mathrm{rp},n}$ and $\bar{\Sigma}_{\boldsymbol{x}_{\mathrm{rp},n}}$ when calculating the matrix products.

3.5.2. Uncertainty propagation for density

The uncertainty propagation for the density observations is straightforward. First, we calculate the Jacobian matrix

$$\boldsymbol{J}_\rho = \partial\rho / \partial \boldsymbol{x}_\rho, \tag{39}$$

where the input parameter vector $\boldsymbol{x}_\rho$ contains the

- mass densities ρ_j of the atmospheric constituents,
- energy accommodation coefficient α_E,
- panel areas A_i,
- panel temperatures T_i,
- atmospheric temperature T_{atm},
- satellite mass m_{sat},
- relative velocity vector $\boldsymbol{v}_{\mathrm{rel}}$, and
- aerodynamic acceleration $\boldsymbol{a}_{\mathrm{aero}}$ in case of density observations derived from accelerometer data or
- averaged aerodynamic acceleration $\bar{\boldsymbol{a}}_{\mathrm{aero}}$ in case of density observations derived from GNSS tracking data.

Again, we presently do not model the uncertainty in the panel normals. The variance of the density observations is then

$$\sigma^2_\rho = \boldsymbol{J}_\rho \Sigma_{\boldsymbol{x}_\rho} \boldsymbol{J}^T_\rho, \tag{40}$$

where $\Sigma_{\boldsymbol{x}_\rho}$ is the input parameter covariance matrix. When constructing the latter, we specify the variance of the atmospheric temperature T_{atm} and mass densities ρ_j as fractions of the signal, in the same way as for the radiation fluxes. Further, we consider the input parameters to be uncorrelated, except for the aerodynamic acceleration $\boldsymbol{a}_{\mathrm{aero}}$ and the averaged aerodynamic acceleration $\bar{\boldsymbol{a}}_{\mathrm{aero}}$.

We use the aerodynamic acceleration $\boldsymbol{a}_{\mathrm{aero}}$ when deriving density observations from accelerometer data. In that case, we account for the accelerometer noise and the uncertainties of the accelerometer bias estimation and radiation pressure acceleration. Therefore, the covariance matrix of the aerodynamic acceleration $\boldsymbol{a}_{\mathrm{aero}}$ is

$$\Sigma_{\boldsymbol{a}_{\mathrm{aero}}} = \Sigma_{\mathrm{acc}} + \Sigma_{\mathrm{diff}}(f_b) + \Sigma_{\mathrm{grav}}(T_b) + \Sigma_{\boldsymbol{a}_{\mathrm{rp}}}, \tag{41}$$

where the covariance matrices $\Sigma_{\mathrm{acc}}, \Sigma_{\mathrm{diff}}(f_b)$, and $\Sigma_{\mathrm{grav}}(T_b)$, were defined in Eqs. (18), (24), and (28), and $\Sigma_{\boldsymbol{a}_{\mathrm{rp}}}$ can be extracted from $\Sigma_{\boldsymbol{y}_{\mathrm{rp},n}}$ defined in Eq. (33). When deriving density observations from GNSS tracking data, we use the average aerodynamic acceleration $\bar{\boldsymbol{a}}_{\mathrm{aero}}$, omit the accelerometer noise, and consider a different averaging period T_a instead of the accelerometer bias estimation period T_b. Thus, the covariance matrix of the averaged aerodynamic acceleration $\bar{\boldsymbol{a}}_{\mathrm{aero}}$ is

$$\Sigma_{\bar{\boldsymbol{a}}_{\mathrm{aero}}} = \Sigma_{\mathrm{diff}}(f_a) + \Sigma_{\mathrm{grav}}(T_a) + \Sigma_{\bar{\boldsymbol{a}}_{\mathrm{rp}}}, \tag{42}$$

where $\Sigma_{\mathrm{diff}}(f_a), \Sigma_{\mathrm{grav}}(T_a)$, and $\Sigma_{\bar{\boldsymbol{a}}_{\mathrm{rp}}}$ are defined in Eqs. (24), (28), and (38).

3.6. Sequence of calculation

Since the uncertainty propagation requires a complex sequence of calculations, we outline the most important steps in Fig. 1. First, we have the choice to import real satellite data or generate simulated satellite data. Then, we calculate the radiation pressure and aerodynamic accelerations, and the mass density, which serve as Taylor points in the linearization. Next, we calculate the Jacobian matrix $\boldsymbol{J}_{\mathrm{rp},n}$ and construct the covariance matrix $\Sigma_{\mathrm{rp},n}$. At this point, the calculations for the accelerometer and GNSS tracking data diverge.

For the accelerometer data, the next steps in the calculations are straightforward. First, we perform the uncertainty propagation for the radiation pressure to obtain $\Sigma_{\boldsymbol{y}_{\mathrm{rp},n}}$ and extract the covariance matrix of the radiation pressure acceleration $\Sigma_{\boldsymbol{a}_{\mathrm{rp},n}}$, which is a submatrix of the former. Then, we perform the uncertainty propagation for density using $\Sigma_{\boldsymbol{a}_{\mathrm{aero},n}}$ from Eq. (41) as input.

The uncertainty propagation for GNSS tracking data requires the input variables in a time window covering $2L+1$ epochs to generate the output at the center epoch because of the averaging. Therefore, we store all required input variables from epochs $t_{n-2L}, \ldots, t_n$ and then perform the calculations for epoch t_{n-L}. In this way, we perform the calculations for the GNSS tracking data in parallel to those for the accelerometer data, reducing the runtime of the software. Once the calculations for epoch t_n are completed, we construct covariance matrix $\bar{\Sigma}_{\boldsymbol{x}_{\mathrm{rp},n-L}}$ and calculate the Jacobian matrix $\bar{\boldsymbol{J}}_{\mathrm{rp},n-L}$ to perform the uncertainty propagation for the average radiation pressure acceleration. Next, we perform the uncertainty propagation for density using $\Sigma_{\bar{\boldsymbol{a}}_{\mathrm{aero},n}}$ from Eq. (42) as input.

Finally, we store all variables of interest and create a set of visualizations (see Section 7), which enable us to interpret the results of the uncertainty propagation.

4. Models

As outlined in Section 2.4, we need the atmospheric composition and temperature to calculate the aerodynamic coefficient. Therefore, we need a thermosphere model to specify these quantities. Further, accounting for albedo and Earth radiation pressure requires radiation flux data as explained in Section 2.5. In the following, we introduce the models and data we use for these purposes. They do not have to be very accurate because they will only serve as the Taylor point in the linearization of the nonlinear relationship between the input parameters and the density observations. Further, it is instructive to specify the uncertainty of the density observations as a fraction of the density (cf. Section 1), where we use the thermosphere model to specify the density.

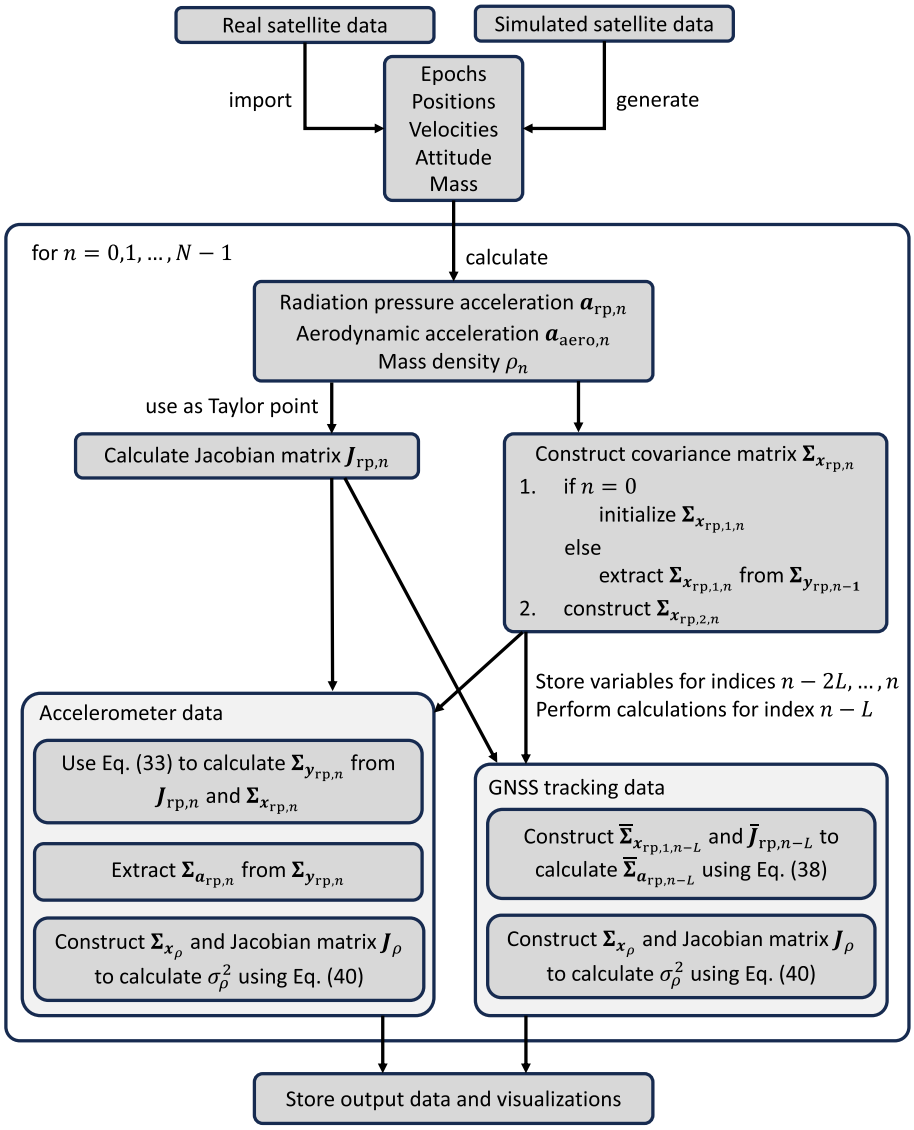

Fig. 1. Flowchart of the most important calculation steps in the uncertainty propagation.

4.1. Atmosphere

We selected the semi-empirical NRLMSISE-00 model to specify the atmosphere because it provides the mass density, mass fraction of eight major atmospheric constituents, and atmospheric temperature in a wide altitude range from the ground to exobase (Picone et al., 2002). Another reason for the selection was convenience since we already had this model integrated into our software. The model inputs are the F10.7 index and its 81-day centered mean as proxies for solar activity, and the 3-hourly ap index and its daily average, the Ap index, indicating the geomagnetic activity.

The NRLMSISE-00 model was constructed using atmospheric composition observations derived from mass spectrometer measurements, thermosphere temperature observations derived from incoherent scatter radar measurements, and molecular oxygen (O2) number density derived from solar ultraviolet occultation data, amongst others. Also, neutral mass density observations derived from the accelerometer measurements and orbital decay data from the 1970s and 1980s were used to construct the model.

While we account for the corotation of the atmosphere as described in Montenbruck and Gill (2012), we presently neglect thermospheric winds when calculating the density observations and only account for their uncertainty when specifying the accuracy of the relative velocity vector. This simplification is justified for the uncertainty propagation because winds are much smaller than the satellite velocity and, consequently, do not significantly change the relative velocity vector. Thus, neglecting winds has no significant effect on the linearization defined in Section 3 because the Taylor point changes only marginally.

4.2. Radiation flux

We use the radiation flux data of the Clouds and the Earth's Radiant Energy System (CERES) project's Energy

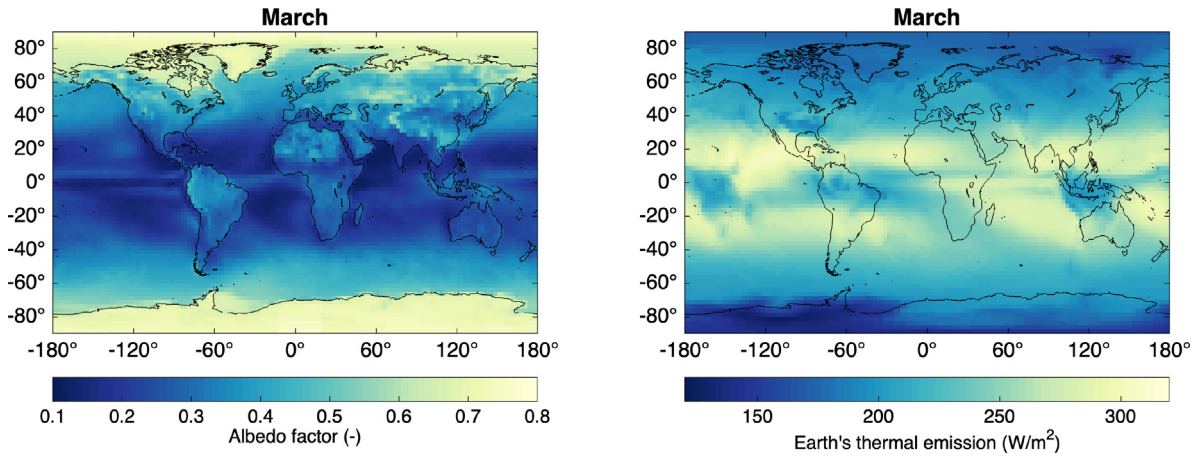

Fig. 2. Maps of the albedo factors (left) and Earth's thermal emission (right) for the month of March.

Balanced and Filled (EBAF) Top-Of-Atmosphere (TOA) all-sky fluxes, edition 4.2[1] (Loeb et al., 2018; Kato et al., 2018). The data is provided as a time series of monthly averaged maps of the longwave and shortwave flux, covering the period from March 2000 until the present. Instead of using the data directly, we calculated averages for each month (January – December) from the data from March 2000 to December 2022 and resampled them from the original $1^\circ \times 1^\circ$ grid to a $2.5^\circ \times 2.5^\circ$ grid to substantially reduce the data volume. Again, we emphasize that we only need a realistic representation of the radiation fluxes, while their accuracy is uncritical for the uncertainty propagation. For Earth's radiation pressure, we use the longwave flux to represent Earth's thermal emission. For albedo, we divide the shortwave flux by the incoming solar flux to obtain albedo factors, to be consistent with the method by Doornbos et al. (2014). To avoid unrealistically large albedo factors, we set incoming solar flux values to 9 Wm^{-2} whenever they are smaller than that value, avoiding a division by small values. As an example, we show the resulting maps of Earth's thermal emission and albedo factors for the month of March in Fig. 2.

5. GRACE data

We will use one of the GRACE satellites to demonstrate the uncertainty propagation. They were launched in March 2002 into near-circular, polar orbits with a mean altitude just above 500 km, separated by about 220 km along the orbit. The mission objective was to map the temporal variations in Earth's gravity field that can be associated with mass change on or near Earth's surface (Tapley et al., 2004). Although the reentry of the satellites due to natural orbital decay was close, the mission operations ended in October 2017 due to age-related battery issues on the GRACE B satellite. The satellites were equipped with GPS receivers enabling positioning at cm-accuracy and precise accelerometers to measure the non-gravitational accelerations, where the precision of 1 nm s^{-2} was limited by perturbations caused by the satellite system (Flury et al., 2008). The satellites' attitude was tightly controlled for the precise ranging between the satellites. Consequently, the satellites' x-axes were pointing toward the other satellite, i.e. in the flight or anti-flight direction, depending on which satellite was leading, and the z-axes were pointing in the nadir direction, i.e. toward Earth (Bandikova et al., 2019).

We arbitrarily chose the GRACE B satellite, for which we retrieved the satellite position, velocity, attitude, and mass data from the GRACE Level 1B data repository[2]. The calibrated accelerations are taken from Siemes et al. (2023).

In this study, we use the panel model provided by Bettadpur (2012), supplemented with the thermal model described by Siemes et al. (2023). The panel model parameters are listed in Table 1. The heat capacity of the satellite body was set to $C_{\mathrm{body}} = 100\ \mathrm{kJK}^{-1}$ and the satellite's internal heat generation to $\dot{Q}_{\mathrm{gen}} = 70$ W. Further, we note that $c_{w,\mathrm{s},k} = 1 - c_{w,\mathrm{a},k} - c_{w,\mathrm{d},k}$ and that the panels' normal vectors are defined in the satellite body frame. We use the energy accommodation coefficient $\alpha_E = 0.85$ proposed by March et al. (2021) for all panels.

We selected November 2003 and November 2008 as periods for demonstration. In November 2003, the mean altitude of the GRACE satellites was 490 km, and solar activity was high, with an average F10.7 index of 141. In November 2008, the mean altitude of 476 km was only slightly lower, whereas solar activity was very low, with an average F10.7 index of 69. Thus, these periods are characterized by solar maximum and minimum conditions while the satellite orbited at similar altitudes. These con-

[1] CERES data is available on the CERES webpage: https://ceres.larc.nasa.gov/data/

[2] GRACE Level 1B data is available on NASA JPL's Physical Oceanography Distributed Active Archive Center: https://podaac.jpl.nasa.gov/

Table 1
GRACE panel model (Bettadpur, 2012), supplemented with thermal model parameters (Siemes et al., 2023). The heat capacity of the satellite body is set to 100 kJ K^{-1} and the satellite internal heat generation to 70W.

Panel	Front	Rear	Starboard	Port	Nadir	Zenith
Panel ID, i	1	2	3	4	5	6
Material ID, m	1	1	2	2	3	2
Area, A_i (m^2)	0.955	0.955	3.155	3.155	6.071	2.167
Normal vector, $\boldsymbol{n}_i$	$\begin{bmatrix}1\\0\\0\end{bmatrix}$	$\begin{bmatrix}-1\\0\\0\end{bmatrix}$	$\begin{bmatrix}0\\0.7660\\-0.6428\end{bmatrix}$	$\begin{bmatrix}0\\-0.7660\\-0.6428\end{bmatrix}$	$\begin{bmatrix}0\\0\\1\end{bmatrix}$	$\begin{bmatrix}0\\0\\-1\end{bmatrix}$
Visible light						
Absorption, $c_{\mathrm{v,a},m}$ (-)	0.34	0.34	0.65	0.65	0.12	0.65
Diffuse reflection, $c_{\mathrm{v,d},m}$ (-)	0.40	0.40	0.05	0.05	0.68	0.05
Infrared radiation						
Absorption, $c_{\mathrm{i,a},m}$ (-)	0.62	0.62	0.81	0.81	0.75	0.81
Diffuse reflection, $c_{\mathrm{i,d},m}$ (-)	0.23	0.23	0.03	0.03	0.19	0.03
Initial temperature, T_i (K)	300	300	300	300	300	300
Heat conductivity, k_i (W K^{-1})	0.1	0.1	0.1	0.1	0.5	0.1
Heat capacitance, C_i (J K^{-1})	1000	1000	5000	5000	10000	5000

trasting conditions enable us to highlight the influence of solar radiation pressure modeling errors and GNSS tracking noise on the density observation uncertainty, aspects that were not treated thoroughly in the preceding studies by Bruinsma and Biancale (2003), Sutton et al. (2007), and Doornbos et al. (2010) as they focused on high solar activity and a satellite orbiting at lower altitudes. The local time of the orbit's ascending node was about 15h in November 2003 and 23h in November 2008, i.e. the GRACE satellites make eclipse transitions during both periods. Further criteria for selecting these periods encompass the radio occultation instrument operations, satellite temperature control, the presence of data gaps, and the absence of satellite maneuvers.

6. Input parameter uncertainty

We need to define realistic uncertainty values for the input parameters to obtain realistic uncertainty values for the density observations. Table 2 lists the values we use in this study. We group the values into three categories: measurement noise, radiation pressure, and aerodynamics. In Section 7, we will investigate how much each category contributes to the uncertainty of the density observations.

The precision of the accelerometer measurements is about 1nm s^{-1}, limited by perturbations stemming from the satellite (Flury et al., 2008). The orbit accuracy is set to 1.2cm in each direction, based on a comparison of the precise orbit of the Level 1B data and our own precise orbit. The position error in the cross-track direction is assumed to be uncorrelated to the error in the along-track and vertical directions. However, the position errors in the along-track and vertical directions are highly correlated (van Helleputte et al., 2009), which we account for by setting the correlation coefficient to 0.9. Further, we assume a temporal correlation by setting $\alpha = -0.4$, justified by the results presented in Section 7.1. Since the accelerometer bias has been estimated daily, $T_b = 1\mathrm{d}$. For the density observations derived from GNSS tracking data, we assume averaging periods of one-third and one orbit to demonstrate the effect of different averaging periods. Further, the sampling frequency of the GNSS tracking is $f_s = 0.1$ Hz.

Since high-fidelity satellite geometry models are available for the GRACE satellites (Mehta et al., 2013; March et al., 2019), we set the uncertainty of the panel areas to 2%. At the current stage of development, we assume that the normal vector is free of errors. Also, the satellite mass is well-known, as the satellite mass, with and without fuel, was accurately determined before launch. The main uncertainty is then related to the uncertainty in propellant consumption, where we assume an uncertainty of 2 kg, which is conservative considering the total amount of 15 kg propellant.

Since the thermal model was determined empirically (Siemes et al., 2023), we set the uncertainty of the heat capacitances (C_i and C_{body}) and heat conductivities (k_i) to 20%. This value can be easily updated once we gain better insight into the accuracy of the thermal model, which is subject to an ongoing investigation. The initial uncertainty in the temperatures (T_i and T_{body}) is of subordinate importance because their influence fades away as we propagate the temperatures and their uncertainties over time. The absorption and reflection coefficients have an uncertainty of about 10%, which is supported by the findings of Siemes et al. (2023). Further, we set the solar flux uncertainty to 0.1% because the solar radiation flux is near-constant and accurately known (Dewitte and Clerbaux, 2017). The radiation fluxes due to albedo and Earth radiation are less accurately known. Therefore, we set their uncertainty to 10%, which we interpret as a conservative assumption (Loeb et al., 2018).

Thermosphere models have an uncertainty of a few tenths in predicting the mass density (Bruinsma et al., 2018). Therefore, we set the uncertainty of the atmospheric temperature and mass density per constituent to 20%. We

Table 2
Uncertainty specification for the input parameters, which are grouped into three categories: measurement noise, radiation pressure, and aerodynamics.

Category and parameter groups	Uncertainty specification
Measurement noise	
Accelerometer (satellite frame)	$\sigma_{\mathrm{acc},x} = 1\mathrm{nms}^{-2}$, $\sigma_{\mathrm{acc},y} = 1\mathrm{nms}^{-2}$, $\sigma_{\mathrm{acc},z} = 1\mathrm{nms}^{-2}$
GNSS-tracking (local orbit frame)	$\sigma_{\mathrm{pos},x} = 1.2\mathrm{cm}$, $\sigma_{\mathrm{pos},y} = 1.2\mathrm{cm}$, $\sigma_{\mathrm{pos},z} = 1.2\mathrm{cm}$
	$\rho_{\mathrm{diff},xy} = 0$, $\rho_{\mathrm{diff},xz} = 0.9$, $\rho_{\mathrm{diff},yz} = 0$, $\alpha = -0.4$
Averaging for accelerometer bias	$T_b = 1\mathrm{d}$
Averaging for GNSS tracking	$T_a = 0.33$ orbits and $T_a = 1.0$ orbit
Sampling frequency of GNSS tracking	$f_s = 0.1\mathrm{Hz}$
Radiation pressure	
Satellite	$\sigma_{A_i} = \frac{1}{50}A_i$, $\sigma_{m_{\mathrm{sat}}} = 2\mathrm{kg}$
Thermal model	$\sigma_{k_i} = \frac{1}{5}k_i$, $\sigma_{C_i} = \frac{1}{5}C_i$, $\sigma_{C_{\mathrm{body}}} = \frac{1}{5}C_{\mathrm{body}}$
	$\sigma_{\dot{Q}_{\mathrm{body}}} = \frac{1}{5}\dot{Q}_{\mathrm{body}}$, $\sigma_{T_i(t_0)} = 10\mathrm{K}$, $\sigma_{T_{\mathrm{body}}(t_0)} = 20\mathrm{K}$
Absorption and reflection coefficients	$\sigma_{c_{\mathrm{v,a},i}} = 0.1$, $\sigma_{c_{\mathrm{v,d},i}} = 0.1$, $\sigma_{c_{\mathrm{v,s},i}} = 0.1$
	$\sigma_{c_{\mathrm{i,a},i}} = 0.1$, $\sigma_{c_{\mathrm{i,d},i}} = 0.1$, $\sigma_{c_{\mathrm{i,s},i}} = 0.1$
Radiation fluxes	$\sigma_{\Phi_{\mathrm{sr}}} = \frac{1}{1000}\Phi_{\mathrm{sr}}$, $\sigma_{\Phi_{\mathrm{alb},k}} = \frac{1}{10}\Phi_{\mathrm{alb},k}$, $\sigma_{\Phi_{\mathrm{er},k}} = \frac{1}{10}\Phi_{\mathrm{er},k}$
Aerodynamics	
Satellite	$\sigma_{A_i} = \frac{1}{50}A_i$, $\sigma_{m_{\mathrm{sat}}} = 2\mathrm{kg}$
Gas-surface interaction	$\sigma_{T_{\mathrm{atm}}(t_n)} = \frac{1}{5}T_{\mathrm{atm}}(t_n)$, $\sigma_{\rho_j(t_n)} = \frac{1}{5}\rho_j(t_n)$, $\sigma_{\alpha_E} = 0.05$
Relative velocity (satellite frame)	$\sigma_{v_{\mathrm{rel},x}} = 50\mathrm{ms}^{-1}$, $\sigma_{v_{\mathrm{rel},y}} = 50\mathrm{ms}^{-1}$, $\sigma_{v_{\mathrm{rel},z}} = 10\mathrm{ms}^{-1}$

assume an uncertainty of 0.05 for the energy accommodation coefficient, which is an optimistic assumption considering the satellite altitude of the test months and the results by Bernstein and Pilinski (2022). Although we neglect wind when calculating density (cf. Section 4), we do consider the uncertainty of models that could be used to account for wind, such as the Horizontal Wind Model by Drob et al. (2015). The uncertainty of the wind model is included in the standard deviation of the relative velocity vector, which we set to 50 m s^{-1} for the horizontal (x and y) components and 10 m s^{-1} for the vertical (z) component. More research is required to replace these rather simple assumptions with a more complex and substantiated approach to specify the uncertainty of the atmospheric temperature, composition, and wind obtained from thermosphere models.

7. Results and discussion

7.1. Aerodynamic acceleration from accelerometer and GNSS-tracking data

First, we compare the aerodynamic acceleration derived from the accelerometer and GNSS tracking data, which gives insight into how appropriate the noise modeling is for the GNSS tracking data. We obtained the aerodynamic acceleration derived from the GNSS tracking data with the Kalman smoother described by van den IJssel et al. (2020). In this approach, the aerodynamic acceleration is modeled as a first-order Gauss–Markov process, defined by a steady-state variance, process noise variance, and correlation time. We selected a correlation time of 5400s for the along-track direction and 360s for the cross-track and radial directions. While van den IJssel et al. (2020) used constant values for the process noise variance, we applied variable values for the along-track direction to account for the large variations in the aerodynamic acceleration that the GRACE satellites experienced during their mission lifetime. Here, we set the process noise variance equal to the daily variance of the along-track aerodynamic acceleration deduced from the NRLMSISE-00 model using Eq. (6), which ensures that the Kalman smoother automatically adapts to the aerodynamic acceleration signal size. For the cross-track and radial directions, we maintained the same constant value of 5 nm s^{-2} for the process noise standard deviation as used by van den IJssel et al. (2020). Fig. 3 shows the Amplitude Spectral Density (ASD), i.e., the square root of the PSD, of the aerodynamic acceleration signal together with the double-differentiation and gravity vector evaluation noise. Since the accelerometer biases are estimated daily using the same GNSS tracking data, the assessment is limited to periods shorter than one day.

The aerodynamic acceleration derived from the accelerometer data (blue curve, partially hidden by the yellow curve above 0.5 mHz and the red curve below) reflects the signal over the entire frequency range. In contrast, the aerodynamic acceleration derived from the GNSS tracking data (red curve) is low-pass filtered due to the Kalman smoother used to obtain the acceleration (van den IJssel et al., 2020), which causes the ASD to drop at frequencies higher than 0.5 mHz, meaning that the high-frequency signal content has been filtered out. Therefore, the difference in the aerodynamic acceleration derived from the accelerometer and GNSS tracking data (yellow curve) closely follows the accelerometer data at high frequencies. At frequencies lower than 0.5 mHz, the difference drops to about 1×10^{-7} m s^{-2} $Hz^{-0.5}$, which is well above the accelerometer precision of 1×10^{-9} m s^{-2} $Hz^{-0.5}$ and the size of the radiation pressure acceleration (cf. Fig. 4). Thus, it largely reflects noise in the GNSS tracking data below that frequency.

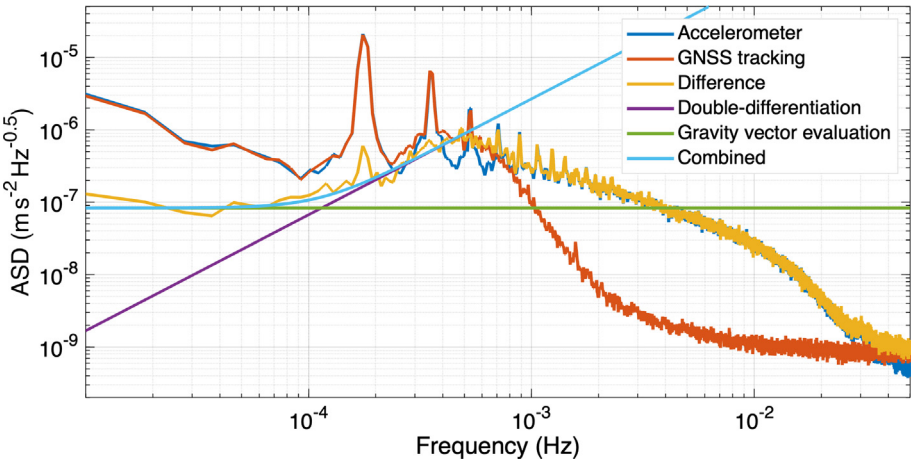

Fig. 3. Aerodynamic accelerations derived from the accelerometer and GNSS tracking data, their difference, and the noise model for accelerations derived from GNSS tracking data, assuming 2.5 cm position noise, a 1 Hz sampling frequency, and a noise shape parameter $\alpha = -0.2$.

The ASD of the double-differentiation noise (purple curve) and gravity vector evaluation noise (green curve) and their combined effect (cyan curve) are shown for reference. At frequencies below 0.1 mHz, the ASD of the difference matches very well the ASD of the gravity vector evaluation noise. In the frequency range from 0.1 mHz to 0.5 mHz, we observe an increase in the ASD of the difference, which closely follows the ASD of the double-differentiation noise. Thus, double-differentiation and gravity vector evaluation noise play important roles in modeling the noise in the aerodynamic acceleration derived from GNSS tracking data.

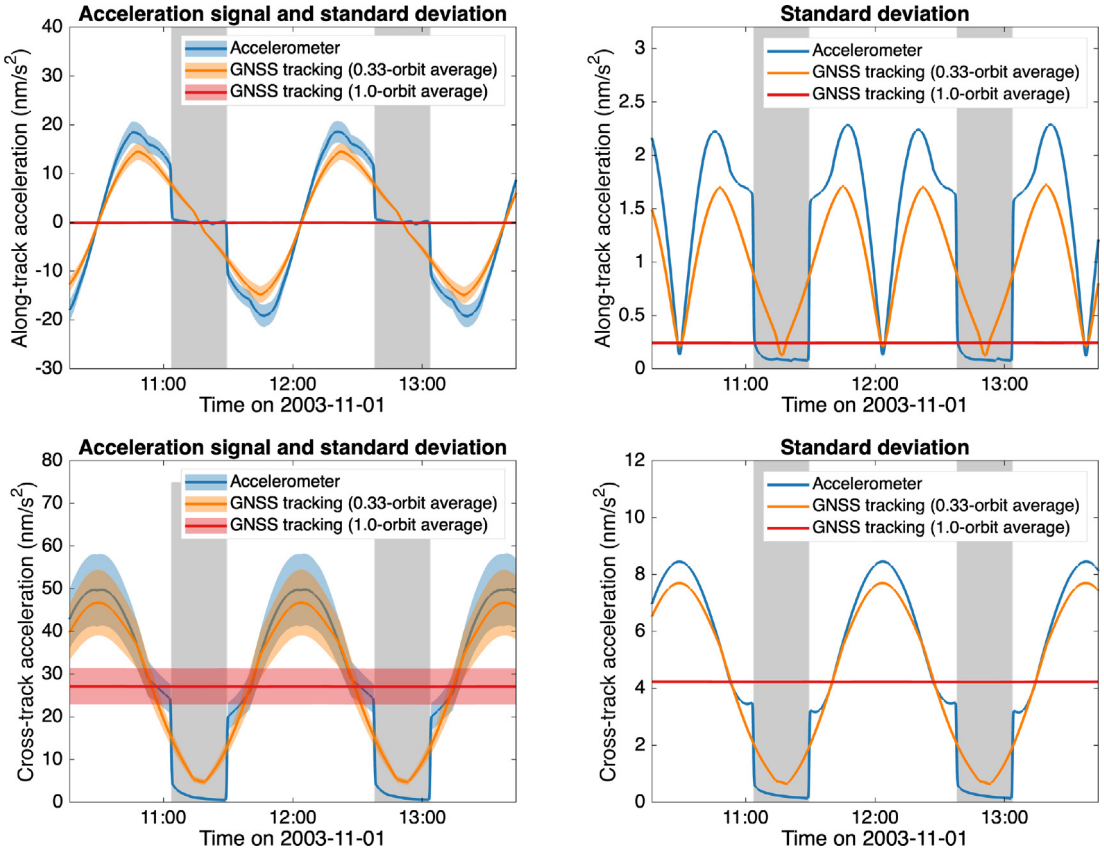

Fig. 4. Radiation pressure acceleration (solid lines) and its standard deviation (shaded areas) in the along-track (top left) and cross-track directions (bottom left). For improved readability, the standard deviations are presented separately in the right column. The grey-shaded areas indicate when the satellite traverses Earth's umbra.

Fig. 3 allows us to determine the along-track resolution of the aerodynamic acceleration and, hence, the density observations derived from GNSS tracking data. We clearly see a sequence of spikes at harmonics of the orbital frequency of about 0.18 mHz. These spikes largely reflect the aerodynamic acceleration signal variation due to dayside-nightside differences in density and density changes due to altitude variations. The accelerations derived from the accelerometer and GNSS tracking data agree well at the first three orbital harmonics (peaks in red and blue curves agree), but starting at the fourth orbital harmonic, the GNSS tracking data does not capture the signal anymore. Therefore, the along-track resolution is 3.5 times the orbital period of 95 min, i.e. 27 min or about 12000 km. This along-track resolution is specific to the conditions experienced by the GRACE B satellite in November 2003. The conditions, particularly the density and altitude, will change over time, leading to a varying along-track resolution.

Further, the combined noise from the double-differentiation and gravity vector evaluation is still lower than the acceleration signal at the third orbital harmonic but larger at the fourth. On the one hand, this means that the Kalman smoother settings were selected optimally to suppress GNSS tracking noise. On the other hand, we may calculate the aerodynamic acceleration signal ASD using a thermosphere model and compare that to the noise ASD of the accelerations derived from GNSS tracking data to predict the achievable along-track resolution of density observations derived from GNSS tracking data.

7.2. Radiation pressure and averaging

We show the radiation pressure acceleration as solid lines and its uncertainty (one standard deviation) as shaded areas for two arbitrary orbits on 1 November 2003 in Fig. 4, in the left column. For better readability, we show the standard deviation of the radiation pressure acceleration in the right column. The grey-shaded areas indicate when the satellite traverses Earth's umbra, whereas it is in sunlight otherwise.

First, we discuss the acceleration in the along-track direction (top left panel), which varies between -20 nm s^{-2} and 20 nm s^{-2}. When no averaging is applied (blue curve), the standard deviation reaches 2.3 nm s^{-2} on the dayside and drops to 0.1 nm s^{-2} on the nightside. The fact that the standard deviation does not drop to zero is largely due to the front and rear panels' temperatures, which only gradually reduce as heat is emitted. Consequently, the uncertainty in the thermal emission acceleration remains notable as the satellite traverses Earth's umbra. We can see this effect even better in the standard deviation of the cross-track acceleration (bottom right panel).

When averaging over one-third of an orbit (orange curve), the peak values in the standard deviation reduce to 1.7 nm s^{-2}, however, at the cost of increased uncertainty in the umbra due to the averaging. These standard deviations are in good agreement with the results for the Swarm satellites presented by van den IJssel et al. (2020), who assessed that the solar radiation pressure acceleration in the along-track acceleration has an accuracy of 2.6 nm s^{-2}. The slightly larger standard deviation for the Swarm satellites can be explained by their more complex geometry compared to the GRACE satellites, noting that van den IJssel et al. (2020) used a panel model to represent the geometry.

In contrast, the acceleration and, consequently, its standard deviation reduce substantially when averaging over one orbit. The latter reduces to a constant value of about 0.2 nm s^{-2}. We also tested averaging over four orbits (not shown), for which one might suspect a further decrease in standard deviation. However, the standard deviation was virtually identical to the case of averaging over one orbit, meaning that some radiation pressure acceleration modeling errors do not average out. This is due to errors, e.g., in the absorption coefficient for visible light, which are treated as uncorrelated errors in the thermal model. This reflects reality well, as the front and rear panels of the GRACE satellites are not identical. Since one panel hosts the K-band ranging antenna and the other the radio occultation antenna, we should expect different errors for the front and rear panels that will not cancel when averaging over one orbit, even when employing accurate radiation pressure modeling as described by Siemes et al. (2023).

The acceleration in the cross-track direction (bottom left panel) ranges from 0 nm s^{-2} and 60 nm s^{-2}. Therefore, averaging will not result in a close-to-zero acceleration, as was the case for the along-track acceleration. Consequently, averaging over one orbit does not substantially reduce the standard deviation, which remains at a constant value of 4.2 nm s^{-2}.

7.3. Density from accelerometers and GNSS-tracking

The effect of averaging on the density observations is illustrated in Fig. 5. The solid lines represent the simulated density based on the thermosphere model and GRACE B orbit, attitude, and mass data, while the shaded areas in the same color indicate the uncertainty (one standard deviation). The grey-shaded areas show when the satellite transits Earth's umbra. We apply no averaging in the case of accelerometer data and averaging over one-third and one orbit in the case of GNSS tracking data to showcase the trade-off between countering GNSS tracking noise and maximizing the resolution along the orbit. We show results for two arbitrary orbits on 1 November 2003 and 2008 to highlight that this trade-off depends on the density, i.e., on the signal-to-noise ratio rather than solely on the noise.

As supporting information, Fig. 6 shows the standard deviation as a percentage of the density for the same two orbits in 2003 and 2008. In addition, the figure illustrates how much aerodynamic and radiation pressure modeling errors and measurement noise contribute to the standard deviation in a stacked representation, i.e., the shaded areas

represent the contribution of these error and noise sources. When a shaded area is much larger than the others, it means that it is the dominating error source. On the contrary, when a shaded area is barely visible, the respective error source is negligible. Table 2 clarifies which parameters contribute to aerodynamic and radiation pressure modeling errors and measurement noise. We note that we include the uncertainty due to incorrectly modeled wind (represented by standard deviations $\sigma_{v_{\mathrm{rel},x}}, \sigma_{v_{\mathrm{rel},y}}$, and $\sigma_{v_{\mathrm{rel},z}}$ in Table 2), which was found to be significant in past studies (Bruinsma and Biancale, 2003; Sutton et al., 2007; Doornbos et al., 2010), into aerodynamic modeling errors.

Inspecting the results for 2003 in Fig. 5, we observe density values in the range from 1.1×10^{-12} kg m^{-3} to 2.9×10^{-12} kg m^{-3} when no averaging is applied, i.e. for accelerometer data (blue curve). The uncertainty is 4%–4.5% of the density for the accelerometer data and the GNSS tracking data when averaging over one orbit (see Fig. 6), which hints that a common error source dominates. In the case of GNSS tracking data, averaging over one-third orbit, the uncertainty of the density is slightly larger with 5%–7.5% due to a more significant contribution of the measurement noise. Averaging over one-third of the orbit reduces the peak values to 2.4×10^{-12} kg m^{-3} and trough values to 1.3×10^{-12} kg m^{-3}, i.e., extreme values are reduced by 15%–20% due to the averaging. One should expect that such an underestimation of extreme values is more pronounced during geomagnetic storms when the density becomes more variable due to localized heating processes (Lühr et al., 2004). Averaging over one orbit obviously smoothes out density variations shorter than one orbit.

Comparing the results for 2003 and 2008, we first notice that the density values range from 8.0×10^{-14} kg m^{-3} to 3.0×10^{-13} kg m^{-3} in 2008, i.e. the density is ten times smaller than in 2003. Further, we observe that averaging has the same smoothing effect, reducing the extreme values as in 2003. In the results for 2008, the standard deviation of the accelerometer-derived density observations (blue curve) is more variable. It exceeds 10% of the density in 20-min time windows centered at, e.g., 11:00 and 12:30 and is only 6% outside these time windows (cf. Fig. 6). However, the largest difference is the uncertainty when averaging over one-third orbit (orange-shaded areas), which is roughly ten times larger in the results for 2008 compared to 2003. When averaging over one orbit, the uncertainty in the density is about 6.5% in 2008, which is close to the 4%–4.5% in 2003.

The contributions of the modeling errors and measurement noise sources, visualized in Fig. 6, demonstrate that the uncertainty quantification is intricate. First, we focus on the density observations derived from accelerometer data (top row). The density observations' uncertainty was about 4%–4.5% in 2003 (top left), of which more than 3% can be attributed to aerodynamic modeling errors. GNSS tracking errors contribute 0.2%–0.3% via the accelerometer bias estimation, and radiation pressure modeling errors account for another 0.5% when the satellite is illuminated by the Sun and 0% otherwise. We may also note that radiation pressure errors make no contribution in the center of the time window when the satellite is in the Sun. That can be explained by the Sun being in the plane perpendicular to the flight direction and, hence, the radiation pressure acceleration being zero in the flight direction. Thus, aerodynamic modeling errors are the dominating error source when the GRACE B satellite orbits at an altitude of about 500 km during a period of high solar activity.

These results are consistent with earlier findings by Bruinsma and Biancale (2003), Sutton et al. (2007), and Doornbos et al. (2010), who identified modeling errors in the aerodynamic coefficient vector and thermospheric wind as the most significant error sources for density observations derived from CHAMP accelerometer data. However, these authors predict a larger uncertainty of 10%–15% for the density observations as opposed to the 4%–4.5% in our results. This can be explained by our much more optimistic assumption on the accuracy of the satellite geometry,

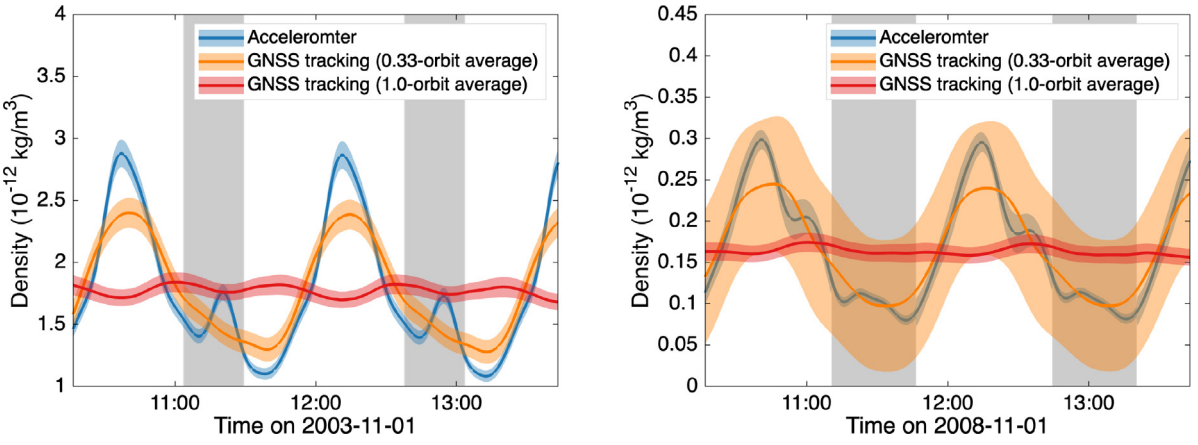

Fig. 5. Density signal along the GRACE B orbit (solid lines) and uncertainty of density observations (color-shaded areas) derived from the accelerometer and GNSS tracking data for two arbitrary orbits on 1 November 2003 (left) and 1 November 2008 (right). The grey-shaded areas indicate when the GRACE B satellite transits Earth's umbra.

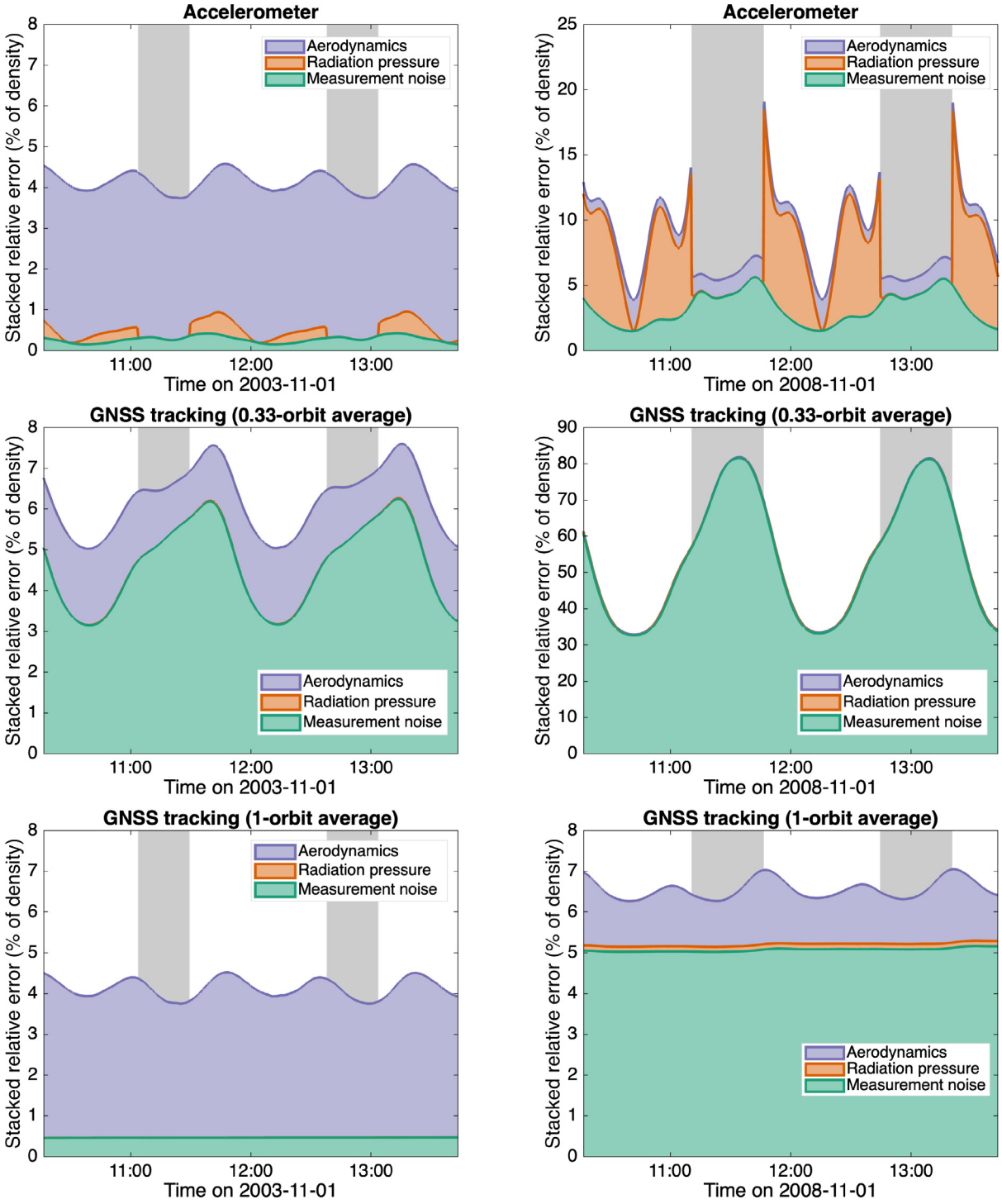

Fig. 6. Standard deviation of density observations derived from the accelerometer (top row) and GNSS tracking data applying averaging over one-third orbit (middle row) and one orbit (bottom row) for two arbitrary orbits on 1 November 2003 (left column) and 1 November 2008 (right column). The standard deviation is expressed as a percentage of the density. The color-shaded areas represent the contribution of aerodynamic and radiation pressure modeling errors and GNSS tracking noise, including accelerometer noise in the top row, in a stacked representation. The grey shaded area indicates when the GRACE B satellite transits Earth's umbra.

justified by high-fidelity modeling as applied by Mehta et al. (2013) and March et al. (2019), whereas the older studies assumed the less accurate panel models (cf. Doornbos et al., 2010). It is worth noting that Sutton et al. (2007) reports that the contribution of radiation pressure modeling errors to the CHAMP density observations' uncertainty is less than 0.54%, which is in perfect agreement with our results for GRACE B.

Examining the uncertainty of density observations in 2008 (top right), when the altitude of GRACE B was still

476 km, but solar activity was very low, we find completely different error and noise contributions. First of all, the uncertainty is 5%–20%, which is substantially larger than the uncertainty in 2003. This large range is caused by the highly variable contribution of radiation pressure modeling errors, which is almost zero when the satellite transits Earth's umbra but makes a peak contribution of 15% when the satellite enters sunlight after transiting Earth's umbra, e.g., at 11:45. Also, GNSS tracking errors contribute 2%–5% as opposed to 0.2%–0.3% in 2003. The larger role of radiation pressure modeling errors and GNSS tracking noise can be explained by the much smaller density in 2008 due to the much lower solar activity, resulting in a much smaller aerodynamic acceleration and, therefore, a much-degraded signal-to-noise ratio for the latter.

Now, we turn our attention to the uncertainty of the density observations derived from GNSS tracking data. When averaging over one-third orbit (middle row), we observe a slightly larger uncertainty of 5%–7.5% in 2003 compared to the results for accelerometer data. However, the contribution of measurement noise, i.e. GNSS tracking noise, is 3%–6%, which is substantially larger than for the density observations derived from accelerometer data. The reason is the much shorter averaging over one-third orbit compared to the daily bias estimation for the accelerometer data. As a side effect of the increased GNSS tracking noise, the relative contribution of radiation pressure modeling errors decreases so much that it becomes negligible. Nevertheless, aerodynamic modeling errors still account for 1.5%–2% of the uncertainty, i.e. approximately a third of the density observations' uncertainty. This balance changes in the results for 2008, where the aerodynamic acceleration is much smaller, leading to a much larger contribution of the GNSS tracking noise. In fact, aerodynamic and radiation pressure modeling errors are completely negligible in this case. Further, the uncertainty in the density observations drastically increased to 33%–82%, which is a consequence of the aerodynamic acceleration being smaller in 2008, while the GNSS tracking noise increased due to the shorter averaging period of one-third orbit, again compared to the daily bias estimation.

By increasing the averaging period to one orbit, we achieve a substantial reduction of GNSS tracking noise because of the shape of the noise PSD (cf. Fig. 3). For the uncertainty of the density observation in 2003, this reduces the contribution of GNSS tracking noise to 0.4%, resulting in an overall uncertainty of about 4%–4.5%, which is very similar to the results for the density observations derived from accelerometer data. For the results for 2008, the overall uncertainty is about 6.2%–7%, which is mostly due to GNSS tracking noise, which contributes slightly more than 5%, while aerodynamic modeling errors account for 1%–1.8%, and radiation pressure errors only 0.1%. Radiation pressure modeling errors play only a minor role in the results in 2003 and 2008 because the averaging over one orbit eliminates them effectively, as demonstrated in Section 7.2.

We may compare our results for GRACE B to those by van den IJssel et al. (2020), who investigated the uncertainty of density observations derived from GNSS tracking data of the Swarm satellites, whose GNSS tracking accuracy, satellite cross-section and mass are similar to those of the GRACE satellites. They assessed that the Swarm B density observations' uncertainty was 7% in April–July 2014, when the satellite was at an altitude of 480 km, which is close to the altitude of the GRACE B satellite. Further, that period was characterized by high solar activity, comparable to the solar activity in 2003. The claimed resolution of the Swarm density observations is about 20min, i.e. approximately 0.2 orbits. Thus, the uncertainty of the GRACE B density observations presented in Fig. 6 in the mid-left panel is representative of the Swarm B density observations' uncertainty. The uncertainty for the GRACE B density observations is 5%–7.5%, which agrees very well with the 7% for Swarm B. The slightly higher uncertainty for Swarm B can be explained by the usage of a panel model for this satellite and the difference in the averaging period. Due to the shorter averaging period for Swarm B, we expect a higher contribution of GNSS tracking noise and, therefore, less accurate density observations. However, we consider the 1% difference in the uncertainties for GRACE B and Swarm B to be marginal.

In April–July 2019, van den IJssel et al. (2020) assessed the uncertainty of the Swarm A and B satellites to be 19% and 60%, respectively. That period coincided with very low solar activity, similar to that in 2008. The altitudes of the Swarm A and B satellites were 440 km and 510 km in that period. Since the altitude of the GRACE B satellite was about 476 km in November 2008, the uncertainty of its density observations should fall within 19%–60%, where we expect a value in the center of that range. However, we find an average uncertainty of 57% when considering averaging over one-third orbit (mid-right panel of Fig. 6), which is very close to the uncertainty of Swarm B. Thus, our results for GRACE B indicate a larger uncertainty than those for Swarm, although the differences are not substantial.

8. Conclusions

We developed a new method that propagates the measurement noise and errors in the satellite specification, thermosphere models, and radiation flux data (cf. Table 2) to the uncertainty of density observations derived from the accelerometer and GNSS tracking data. The software version that was used for this publication has been published on the 4TU.ResearchData repository (Siemes, 2024). The most recent software version is available on the Delft University of Technology GitLab repository (https://gitlab.tudelft.nl/csiemes/usato).

The method can be used for multiple purposes. The most obvious is to supplement the existing density and crosswind datasets derived from the accelerometer and GNSS tracking data, which will be beneficial for data

assimilation and studies in which these data are used as ground truth to validate other data or methods. Further, the method can be used within mission planning for predicting the along-track resolution of density observations derived from GNSS tracking data and studying what limits the density observations' accuracy. Alternatively, the method allows for assessing the value of commercial GNSS data for the purpose of deriving density observations before the purchase.

When analyzing the effect of GNSS tracking noise in Section 7.1, we found that averaging over longer periods reduces the noise as long as differentiation noise dominates. Once the gravity vector evaluation noise is larger than the differentiation noise, averaging over longer periods will reduce the effect of GNSS tracking noise according to the $\sqrt{n}$ law. Therefore, averaging over more than one orbit has only limited benefit, also because radiation pressure modeling errors do not decrease much, as discussed in Section 7.2. This has repercussions for deriving density from satellites orbiting at altitudes above approximately 800 km, noting that this value for the altitude depends on the density and, therefore, solar activity. Further, we found in Section 7.2 that the radiation pressure modeling errors in the cross-track direction do not average out, which makes deriving crosswind observations from GNSS tracking data very challenging.

The uncertainty analysis for density observations derived from accelerometer data in Section 7.3 revealed a good agreement with earlier studies, except that we find a smaller uncertainty due to advances in satellite geometry modeling. While earlier studies focused on the uncertainty of CHAMP and GRACE density observations collected during high solar activity, we included November 2008 as a test period with low solar activity. The GRACE B satellite was still at 476 km altitude, resulting in a much smaller aerodynamic acceleration than during high solar activity earlier in the mission. In these conditions, radiation pressure modeling errors contributed substantially to the uncertainty of the density observations. The aerodynamic acceleration decreases exponentially with altitude while radiation pressure remains constant. Thus, the contribution of radiation pressure modeling errors will exponentially grow with altitude, rendering accelerometer data useless for deriving density observations at altitudes higher than approximately 600 km, at least outside Earth's umbra, even when substantially reducing the accelerometer measurement noise.

Caution must be applied when using density observations derived from GNSS tracking data to study dynamic events such as geomagnetic storms. The unavoidable averaging will reduce the excursion of extreme values from the mean density. Furthermore, this reduction will affect the standard deviation defined by Sutton (2018), which is often used to assess the agreement between density observations and thermosphere models.

Finally, we emphasize that the presented method only propagates the uncertainty of known models and error sources to the uncertainty of the density observations, whereas incorrect models and unknown error sources are not considered. An example is the gas-surface interaction, where we assume a DRIA model, i.e., atmospheric particles are reflected diffusely on the satellite surfaces. If a quasi-specular reflection was closer to physical reality, one could use the model proposed by (Lord, 1991), used by Mehta et al. (2017) to generate density datasets for the CHAMP and GRACE satellites. Consequently, the method may underestimate the uncertainty of density observations, although it is much more sophisticated than earlier methods.

9. Outlook

In its current development state, the method treats errors in atmospheric conditions (temperature, density of constituents, and wind) and gas-surface interaction in a simplistic way. More investigations are needed for more realistic modeling of these error sources, which are likely correlated, and functions of solar and geomagnetic activity, magnetic latitude, and local solar time. Similarly, the accuracy of the radiation fluxes and satellite parameters related to radiation pressure modeling (absorption and reflection coefficients and heat capacitance and conduction parameters) must be investigated to make more realistic assumptions about these noise sources. These investigations will be the next logical step to improve the method, after which it will be extended to quantify the uncertainty of crosswind observations. Once these important steps are completed, the method will be used to augment the existing density and crosswind datasets available on http://thermosphere.tudelft.nl. In this context, we intend to include CERES radiation flux data directly instead of using monthly average maps.

Satellite attitude errors are presently not accounted for since all satellites with accelerometers also have star sensors, leading to such accurate attitude knowledge that attitude errors may be safely neglected (Bruinsma and Biancale, 2003). Nevertheless, accounting for attitude noise is straightforward via specifying the uncertainty in vector $\hat{\boldsymbol{e}}$ in Eq. (7). This will be an important extension for satellites that feature a GNSS receiver but no highly accurate attitude sensor, such as star sensors.

Finally, we found in Section 7.1 that the achievable resolution of density observations derived from GNSS tracking data depends on the signal-to-noise ratio of the aerodynamic acceleration. This motivates an adaptive selection of the averaging period in the method presented by van den IJssel et al. (2020) that will not only depend on the GNSS tracking accuracy but also on the orbit and solar activity.

Declaration of Competing Interest

The authors declare that they have no known competing financial interests or personal relationships that could have appeared to influence the work reported in this paper.

Acknowledgments

The research was performed on request by the Community Coordinated Modeling Center via an agreement with the Universities Space Research Association (USRA).

Appendix A. Aerodynamic coefficient vector

The calculation of the aerodynamic coefficient vector based on the equations provided by Sentman (1961) is explained by Doornbos (2011). We provide here a brief summary of the equations.

The drag and lift coefficients of the i-th panel are

$$C_{\mathrm{drag},i,j} = A_i \left(\frac{1}{\sqrt{\pi}} P_{i,j} + d_i \left(1 + \frac{1}{2S_j^2} \right) Z_{i,j} + \frac{d_i}{2} R_{i,j} \left(d_i \sqrt{\pi} Z_{i,j} \right) + P_{i,j} \right) \tag{A.1}$$

and

$$C_{\mathrm{lift},i,j} = A_i \left(\frac{l_i}{2S_j^2} Z_{i,j} + \frac{l_i}{2} R_{i,j} \left(d_i \sqrt{\pi} Z_{i,j} + P_{i,j} \right) \right), \tag{A.2}$$

respectively, where index j indicates the atmosphere constituent (e.g., atomic oxygen). The parameters $P_{i,j}$ and $Z_{i,j}$ are defined as

$$P_{i,j} = \frac{1}{S_j} \exp(-d_i^2 S_j^2) \tag{A.3}$$

and

$$Z_{i,j} = 1 + \mathrm{erf}(d_i S_j), \tag{A.4}$$

respectively, where 'exp' and 'erf' are the exponential and error functions, respectively. The parameter $R_{i,j}$ is the ratio of reemitted and incident velocity of gas particles, which we calculate according to Koppenwallner (2009):

$$R_{i,j} = \sqrt{\frac{1}{2} + \frac{\alpha_E}{2} \left(\frac{4 R T_i}{m_j \mid \boldsymbol{v}_{\mathrm{rel}} \mid^2} - 1 \right)} \tag{A.5}$$

Here, α_E is the energy accommodation coefficient, $\boldsymbol{v}_{\mathrm{rel}}$ the relative velocity vector, T_i the panel temperature, m_j the molar mass of the atmospheric constituent, and R the gas constant. The other parameters are the speed ratio

$$S_j = \frac{\mid \boldsymbol{v}_{\mathrm{rel}} \mid}{v_{\mathrm{mp},j}}, \tag{A.6}$$

the most probable speed

$$v_{\mathrm{mp},j} = \sqrt{\frac{2 R T_{\mathrm{atm}}}{m_j}}, \tag{A.7}$$

and the negative dot products of the drag and lift vectors, $\hat{\boldsymbol{u}}_{\mathrm{drag}}$ and $\hat{\boldsymbol{u}}_{\mathrm{lift}}$, with the panel normal $\boldsymbol{n}_i$,

$$d_i = -\hat{\boldsymbol{u}}_{\mathrm{drag}} \cdot \boldsymbol{n}_i \tag{A.8}$$

and

$$l_i = -\hat{\boldsymbol{u}}_{\mathrm{lift}} \cdot \boldsymbol{n}_i, \tag{A.9}$$

respectively. The drag and lift vectors of the i-th panel are defined by the panel normal and relative velocity vector:

$$\hat{\boldsymbol{u}}_{\mathrm{drag}} = \frac{\boldsymbol{v}_{\mathrm{rel}}}{\mid \boldsymbol{v}_{\mathrm{rel}} \mid} \tag{A.10}$$

and

$$\hat{\boldsymbol{u}}_{\mathrm{lift},i} = -\frac{(\boldsymbol{v}_{\mathrm{rel}} \times \hat{\boldsymbol{n}}_i) \times \boldsymbol{v}_{\mathrm{rel}}}{\mid (\boldsymbol{v}_{\mathrm{rel}} \times \hat{\boldsymbol{n}}_i) \times \boldsymbol{v}_{\mathrm{rel}} \mid}. \tag{A.11}$$

The aerodynamic coefficient vector is the mass-weighted average of the aerodynamic coefficients for the atmospheric constituents:

$$\boldsymbol{C}_{\mathrm{aero}} = \sum_i \sum_j \frac{\rho_j}{\rho} \left(C_{\mathrm{drag},i,j} \hat{\boldsymbol{u}}_D + C_{\mathrm{lift},i,j} \hat{\boldsymbol{u}}_{\mathrm{lift},i} \right). \tag{A.12}$$

References

Bandikova, T., McCullough, C., Kruizinga, G.L., et al., 2019. GRACE accelerometer data transplant. Adv. Space Res. 64 (3), 623–644. https://doi.org/10.1016/j.asr.2019.05.021.

Bernstein, V., Pilinski, M., 2022. Drag coefficient constraints for space weather observations in the upper thermosphere. Space Weather 20 (e2021SW002977). https://doi.org/10.1029/2021SW002977.

Bettadpur, S., 2012. Gravity recovery and climate experiment: Product specification document. Technical report GRACE 327–720 Center for Space Research. The University of Texas at Austin.

Bruinsma, S., Biancale, R., 2003. Total densities derived from accelerometer data. J. Spacecr. Rock. 40, 230–236. https://doi.org/10.2514/2.3937.

Bruinsma, S., Boniface, C., 2021. The operational and research DTM-2020 thermosphere models. J. Space Weather Space Clim. 11 (47). https://doi.org/10.1051/swsc/2021032.

Bruinsma, S., Doornbos, E., Bowman, B., 2014. Validation of GOCE densities and evaluation of thermosphere models. Adv. Space Res. 54, 576–585. https://doi.org/10.1016/j.asr.2014.04.008.

Bruinsma, S., Siemes, C., Emmert, J.T., et al., 2022. Description and comparison of 21st century thermosphere data. Adv. Space Res. https://doi.org/10.1016/j.asr.2022.09.038.

Bruinsma, S., Sutton, E., Solomon, S.C., et al., 2018. Space weather modeling capabilities assessment: Neutral density for orbit determination at low Earth orbit. Space Weather 16, 1806–1816. https://doi.org/10.1029/2018SW002027.

Calabia, A., Jin, S., & Tenzer, R. (2015). A new GPS-based calibration of GRACE accelerometers using the arc-to-chord threshold uncovered sinusoidal disturbing signal. Aerospace Science and Technology, 45, 265–271. URL: https://www.sciencedirect.com/science/article/pii/S1270963815001601. doi: 10.1016/j.ast.2015.05.013.

Codrescu, S., Codrescu, M., Fedrizzi, M., 2018. An ensemble Kalman filter for the thermosphere-ionosphere. Space Weather 16, 57–68. https://doi.org/10.1002/2017SW001752.

Dewitte, S., Clerbaux, N., 2017. Measurement of the Earth radiation budget at the top of the atmosphere – a review. Remote Sensing 9 (1143). https://doi.org/10.3390/rs9111143.

Doornbos, E., 2011. Thermospheric Density and Wind Determination From Satellite Dynamics. In: Department of Astrodynamics and

Satellite Missions. Delft University of Technology, URL: http://resolver.tudelft.nl/uuid:33002be1-1498-4bec-a440-4c90ec149aea.

Doornbos, E., Bruinsma, S., Fritsche, B. et al. (2014). ESA contract 4000102847/NL/EL, GOCE+ Theme 3: Air density and wind retrieval using GOCE data – Final Report. Technical Report TU Delft. URL: https://earth.esa.int/eogateway/documents/20142/1181177/GOCE-theme-3-final-report.pdf.

Doornbos, E., van den IJssel, J., Lühr, H., et al., 2010. Neutral density and crosswind determination from arbitrarily oriented multiaxis accelerometers on satellites. J. Spacecr. Rock. 47 (4), 580–589. https://doi.org/10.2514/1.48114.

Drob, D.P., Emmert, J.T., Meriwether, J.W., et al., 2015. An update to the horizontal wind model (HWM): The quiet time thermosphere. Earth and Space Science 2, 301–319. https://doi.org/10.1002/2014EA000089.

Flury, J., Bettadpur, S., Tapley, B.D., 2008. Precise accelerometry onboard the GRACE gravity field satellite mission. Adv. Space Res. 42, 1414–1423. https://doi.org/10.1016/j.asr.2008.05.004.

Forootan, E., Farzaneh, S., Kosary, M., et al., 2021. A simultaneous calibration and data assimilation (C/DA) to improve NRLMSISE00 using thermospheric neutral density (TND) from space-borne accelerometer measure. Geophys. J. Int. 224, 1096–1115. https://doi.org/10.1093/gji/ggaa507.

Gondelach, D.J., Linares, R., 2021. Real-time thermospheric density estimation via radar and GPS tracking data assimilation. Space Weather 19 (e2020SW002620). https://doi.org/10.1029/2020SW002620.

He, J., Astafyeva, E., Yue, X., et al., 2023. Comparison of empirical and theoretical models of the thermospheric density enhancement during the 3–4 February 2022 geomagnetic storm. Space Weather 21 (e2023SW003521). https://doi.org/10.1029/2023SW003521.

van Helleputte, T., Doornbos, E., Visser, P., 2009. CHAMP and GRACE accelerometer calibration by GPS-based orbit determination. Adv. Space Res. 43, 1890–1896. https://doi.org/10.1016/j.asr.2009.02.017.

van den IJssel, J., Doornbos, E., Iorfida, E., et al., 2020. Thermosphere densities derived from Swarm GPS observations. Adv. Space Res. 65, 1758–1771. https://doi.org/10.1016/j.asr.2020.01.004.

Kato, S., Rose, F.G., Rutan, D.A. et al. (2018). Surface irradiances of Edition 4.0 Clouds and the Earth's Radiant Energy System (CERES) Energy Balanced and Filled (EBAF) data product. Journal of Climate, 31, 4501–4527. doi:10.1175/JCLI-D-17-0523.1.

Klinger, B., Mayer-Gürr, T., 2016. The role of accelerometer data calibration within GRACE gravity field recovery: Results from ITSG-Grace2016. Adv. Space Res. 458, 1597–1609. https://doi.org/10.1016/j.asr.2016.08.007.

Koppenwallner, G., 2009. Energy accommodation coefficient and momentum transfer modeling. Technical report HTG–TN–08–11 HTG. Technical report HTG–TN–08–11 HTG, Katlenburg, Lindau.

Licata, R.J., Mehta, P.M., Tobiska, W.K., et al., 2021. Qualitative and quantitative assessment of the SET HASDM database. Space Weather, p. 19. https://doi.org/10.1016/10.1029/2021SW002798, e2021SW002798.

Loeb, N.G., Doelling, D.R., Wang, H., et al., 2018. Clouds and the Earth's Radiant Energy System (CERES) Energy Balanced and Filled (EBAF) Top-Of-Atmosphere (TOA) Edition-4.0 data product. J. Clim. 31, 895–918. https://doi.org/10.1175/JCLI-D-17-0208.1.

Lord, R.G., 1991. Some extensions to the Cercignani-Lampis gas–surface scattering kernel. Phys. Fluids A 3 (4), 706–710. https://doi.org/10.1063/1.858076.

Lühr, H., Rother, M., Köhler, W., et al., 2004. Thermospheric up-welling in the cusp region: Evidence from CHAMP observations. Geophys. Res. Lett. 31 (L06805). https://doi.org/10.1029/2003GL019314.

March, G., Doornbos, E., Visser, P., 2019. High-fidelity geometry models for improving the consistency of CHAMP, GRACE, GOCE and Swarm thermospheric density data sets. Adv. Space Res. 63, 213–238. https://doi.org/10.1016/j.asr.2018.07.009.

March, G., van den IJssel, J., Siemes, C., et al., 2021. Gas-surface interactions modelling influence on satellite aerodynamics and thermosphere mass density. J. Space Weather Space Clim. 11 (54). https://doi.org/10.1051/swsc/2021035.

Mehta, P.M., McLaughlin, C.A., Sutton, E.K., 2013. Drag coefficient modeling for GRACE using Direct Simulation Monte Carlo. Adv. Space Res. 52 (12), 2035–2051. https://doi.org/10.1016/j.asr.2013.08.033.

Mehta, P.M., Paul, S.N., Crisp, N.H., et al., 2022. Satellite drag coefficient modeling for thermosphere science and mission operations. Adv. Space Res. https://doi.org/10.1016/j.asr.2022.05.064.

Mehta, P.M., Walker, A.C., Sutton, E.K., et al., 2017. New density estimates derived using accelerometers on board the CHAMP and GRACE satellites. Space Weather 15 (4), 558–576. https://doi.org/10.1002/2016SW001562.

Montenbruck, O., Gill, E., 2012. Satellite Orbits. Springer. https://doi.org/10.1007/978-3-642-58351-3.

Picone, J.M., Hedin, A.E., Drob, D.P. et al. (2002). NRLMSISE-00 empirical model of the atmosphere: Statistical comparisons and scientific issues. Journal of Geophysical Research: Space Physics, 107 (A12)(1468). doi:10.1029/2002JA009430.

Robertson, R.V., 2015. Highly Physical Solar Radiation Pressure Modeling During Penumbra Transitions PhD thesis. Virginia Polytechnic Institute and State University, Blacksburg, Virginia. URL.

Sentman, L.H. (1961). Free molecule flow theory and its application to the determination of aerodynamic forces. Technical Report LOCKHEED MISSILES AND SPACE CO INC SUNNYVALE CA.

Siemes, C., 2024. Uncertainty specification and analysis for thermosphere observations. Version 1. 4TU.ResearchData. Software. https://doi.org/10.4121/08c86d28-e44e-496d-a3b3-185ec43475d4.v1.

Siemes, C., Borries, C., Bruinsma, S., et al., 2023. New thermosphere neutral mass density and crosswind datasets from CHAMP, GRACE, and GRACE-FO. J. Space Weather Space Clim. 13 (16). https://doi.org/10.1051/swsc/2023014.

Smith, S.W., 2003. Digital Signal Processing, A Practical Guide for Engineers and Scientists. Newnes, Amsterdam.

Sutton, E.K., 2018. A new method of physics-based data assimilation for the quiet and disturbed thermosphere. Space Weather 16, 736–753. https://doi.org/10.1002/2017SW001785.

Sutton, E.K., Nerem, R.S., Forbes, J.M., 2007. Density and winds in the thermosphere deduced from accelerometer data. J. Spacecr. Rock. 44 (6), 1210–1219. https://doi.org/10.2514/1.28641.

Tapley, B.D., Bettadpur, S., Watkins, M., et al., 2004. The gravity recovery and climate experiment: Mission overview and early results. Geophys. Res. Lett. 31 (9). https://doi.org/10.1029/2004GL019920.

Teixeira Da Encarnação, J., Save, H., Tapley, B., et al., 2020. Accelerometer parameterization and the quality of Gravity Recovery and Climate Experiment solutions. J. Spacecr. Rock. 57 (4). https://doi.org/10.2514/1.A34639.

Touboul, P., Foulon, B., Christophe, B. et al. (2012). CHAMP, GRACE, GOCE instruments and beyond. In S. Kenyon, M. Pacino, & U. Marti (Eds.), Geodesy for Planet Earth (pp. 215–221). Springer volume 136. doi:10.1007/978-3-642-20338-1_26.

Touboul, P., Métris, G., Sélig, H., et al., 2016. Gravitation and geodesy with inertial sensors, from ground to space. Aerospace Lab, 12. https://doi.org/10.12762/2016.AL12-11 (AL12-11).